Large Destabilization of (TiVNb)-Based Hydrides via (Al, Mo) Addition: Insights from Experiments and Data-Driven Models

Nayely Pineda Romero, Matthew Witman, Kim Harvey, Vitalie Stavila, V. Nassif, Erik Elkaïm, Claudia Zlotea

To cite this version:

Nayely Pineda Romero, Matthew Witman, Kim Harvey, Vitalie Stavila, V. Nassif, et al.. Large Destabilization of (TiVNb)-Based Hydrides via (Al, Mo) Addition: Insights from Experiments and Data-Driven Models. ACS Applied Energy Materials, 2023, 6 (24), pp.12560-12572. ⟨10.1021/acsaem.3c02696⟩. ⟨hal-04389948⟩

HAL Id: hal-04389948
https://hal.science/hal-04389948v1

Submitted on 12 Jan 2024

Large destabilization of (TiVNb)-based hydrides via (Al, Mo) addition: insights from experiments and data-driven models

*Nayely Pineda Romero[1], Matthew Witman[2], Kim Harvey[2], Vitalie Stavila[2], Vivian Nassif[3], Erik Elkaïm[4] and Claudia Zlotea[1]**

[1]Univ Paris Est Creteil, CNRS, ICMPE, UMR 7182, 2 rue Henri Dunant, 94320 Thiais, France

[2]Sandia National Laboratories, Livermore, CA, 94551, United States.

[3]University Grenoble Alpes, CNRS, Grenoble INP, Institut Néel, 38000 Grenoble, France.

[4]Synchrotron SOLEIL, L'Orme des Merisiers, Saint-Aubin, BP48, 91192 Gif sur Yvette, France.

ABSTRACT

High entropy alloys (HEAs) represent an interesting alloying strategy that can yield exceptional performance properties needed across a variety of technology applications, including hydrogen storage. Examples include ultra-high volumetric capacity materials (BCC alloys → FCC dihydrides) with improved thermodynamics relative to conventional high-capacity metal hydrides (like MgH_2), but still further destabilization is needed to reduce operating temperature and increase systems-level capacity. In this work, we demonstrate efficient hydride destabilization strategies by synthesizing two new $Al_{0.05}(TiVNb)_{0.95-x}Mo_x$ (x=0.05, 0.10) compositions. We specifically evaluate the effect of Molybdenum (Mo) addition on the phase structure, microstructure, hydrogen absorption and desorption properties. Both alloys crystallize in a *bcc* structure with decreasing lattice parameters as the Mo content increases. The alloys can rapidly absorb hydrogen at 25 °C with capacities of 1.78 H/M (2.79 wt.%) and 1.79 H/M (2.75 wt.%) with increasing Mo content. Pressure-composition-isotherms suggest a two-step reaction for hydrogen absorption to a final *fcc* dihydride phase. The experiments demonstrate that increasing Mo content results in a significant hydride destabilization, which is consistent with predictions from a gradient boosting tree data-driven model for metal hydride thermodynamics. Furthermore, improved desorption properties with increasing Mo content and reversibility were observed by *in situ* synchrotron X-ray diffraction, *in situ* neutron diffraction, and thermal desorption spectroscopy.

KEYWORDS

High entropy alloys; Hydrogen absorption/desorption; *In situ* synchrotron X-Ray diffraction; *In situ* neutron diffraction; thermodynamics.

1. INTRODUCTION

Clean hydrogen has the potential to play an important role in decarbonizing economic sectors with difficult-to-abate emissions. However, the low volumetric energy density (9.9 MJ/m^3) of hydrogen presents a major challenge for its storage [1–4]. Among the different hydrogen storage techniques, metal hydrides are considered a promising option for a variety of reasons, including lower operating pressures and higher volumetric densities than 700 bar compressed gas. Nonetheless, the gravimetric capacities of intermetallic compounds and body-centered cubic (*bcc*) alloys remain low (about 2 wt.%), whereas light metal hydrides, such as MgH_2 with high capacity of 7.6 wt.%, typically require high temperatures for desorption which represents an obstacle for practical use [5–7]. In addition, the use of lightweight, earth-abundant materials in interstitial hydrides has been considered to achieve high hydrogen uptake and thus be usable for on-board vehicles [8].

Recently, high-entropy alloys (HEAs) have been introduced as promising materials for hydrogen storage due to interesting properties, such as exceptional capacity ($H/M > 2$) with desorption enthalpies less than conventional materials (*e.g.*, MgH_2) [9]. HEAs (≥ 5 principal elements in the range of 5-35 at.%) or multi-principal element alloys (MPEAs) with no restrictions on the number of elements form random solid solutions instead of phase-separated intermetallic compounds partly due to the stabilization effect of high mixing entropy [10]. Moreover, the solid solutions crystallize as simple body-centered cubic (*bcc*), face-centered cubic (*fcc*), or hexagonal close-packed (*hcp*) lattices. Attempts have been made to predict the formation and stability of such phases by different empirical parameters and to obtain rational theoretical design rules with varying degrees of success. Examples include the lattice distortion (δ) caused by the mismatch between different atomic sizes of the constituents, the valence electron concentration (VEC), the mixing enthalpy/entropy, or the entropy to enthalpy ratio (Ω) [11–14]. Furthermore, the properties of

HEAs can be related to four core effects (cocktail effect, high entropy, sluggish diffusion and lattice distortion) [15].

Consequently, there is now a push to rationally design HEAs for hydrogen storage that can maximize capacity while minimizing desorption enthalpy (and required desorption temperature) [8,16]. A number of HEAs with *bcc* structure possess outstanding volumetric hydrogen capacities, as reported for TiVZrNbHf [9], $TiVZrNbHf_{0.5}$ [17], TiZrNbHfTa [18] and $Ti_4V_3NbCr_2$ [19]. The inclusion of lightweight elements (such as Mg, Al) to improve gravimetric capacities has also been explored [20]. For example, $Mg_{35}Al_{15}Ti_{25}V_{10}Zn_{15}$ achieves a high capacity of 2.3-2.7 wt.% depending on the method of synthesis (arc melting or reactive ball milling) and forms a mixture of hydrides with desorption temperatures above 300 °C [21]. Montero *et al.* reported a capacity of 2.7 wt.% for $Mg_{0.10}Ti_{0.30}V_{0.25}Zr_{0.10}Nb_{0.25}$ with an improvement in the cycling properties compared to the quaternary alloy without Mg [22]. Al incorporation in $Al_{0.10}Ti_{0.30}V_{0.25}Zr_{0.10}Nb_{0.25}$ yields a capacity of 2.6 wt.% with improvements in both cycling properties and desorption temperature [23]. In recent work, we proposed the *bcc* $Al_{0.05}(TiVNb)_{0.95}$ as a promising material after systematically studying the influence of Al addition in the equimolar TiVNb [24]. We demonstrated a destabilization of the hydride, better desorption properties, improved reversible capacity during cycling, and a saturation capacity of 2.96 wt.% for the $Al_{0.05}(TiVNb)_{0.95}$ composition [24].

These developments in high-capacity, lightweight, thermodynamically destabilized HEAs motivate continuous work to further increase their performance as materials for real world (*e.g.*, stationary) storage applications. Nonetheless, further control in tuning the thermodynamics of the hydride formation (*i.e.*, increasing the phase-change/plateau pressure by reducing the enthalpy of desorption or increasing the entropy of desorption) is desired to improve their practical use as hydrogen storage materials. Despite its low hydrogen affinity and relative important weight, Molybdenum (*bcc* structure) has a significant potential to stabilize the *bcc* phases [25,26] and consequently to destabilize the related hydrides [27]. Shen *et al.* reported an increase in gravimetric capacity using up to 10 at.% Mo in the $Ti_{0.20}Zr_{0.20}Hf_{0.20}Mo_{0.10}Nb_{0.30}$ composition (1.54 wt.%) compared to $Ti_{0.20}Zr_{0.20}Hf_{0.20}Nb_{0.40}$ (1.12 wt.%), as well as a decrease in thermal stability (reduction in the desorption temperature) with increasing Mo content, which was attributed to the smaller cell volume and weaker H-metal bonding [26]. Similarly, Bouzidi *et al.* reported $Ti_{0.30}V_{0.25}Zr_{0.10}Nb_{0.25}Mo_{0.10}$ with an increased gravimetric capacity (2.8 wt.%) as compared to the alloy without Mo (2.47 wt.%) [28], a decrease in the desorption temperature, and a good reversibility during absorption/desorption cycling [29].

Here we extend this design strategy, *i.e.* the addition of Mo into $Al_{0.05}(TiVNb)_{0.95}$, one of our most promising compositions to date, will be thoroughly studied. Based on chemical intuition and corroborated by data-driven modeling predictions of hydride thermodynamics, we hypothesize that the hydride phase can be still further destabilized (decrease in desorption temperature) with small amounts of Mo addition. Therefore, we synthesize and characterize the hydrogen storage properties of $Al_{0.05}(TiVNb)_{0.95-x}Mo_x$ (x=0.05, 0.10) as determined by several hydrogen absorption/desorption techniques along with detailed structural characterization by *in situ* synchrotron X-ray diffraction and *in situ* neutron diffraction. We rationalize the role of Mo addition in different concentrations and its effect on the crystal structure, microstructure, and hydrogen sorption properties. These results elucidate an effective design strategy for destabilizing HEAs while maintaining high hydrogen capacity.

2. EXPERIMENTAL SECTION

The $Al_{0.05}(TiVNb)_{0.95-x}Mo_x$ (x = 0.05, 0.10) compositions were synthetized by high-temperature arc melting from bulk pieces of Ti (99.99%, Alfa Aesar), V (99.9%, NEYCO Vacuum&Materials), Nb (99.95%, Alfa Aesar), Al (99%, STREM Chem) and Mo (99.9%, ChemPur). The synthesis begins with the formation of the TiVNb-Mo pre-alloy under Ar atmosphere (about 300 mbar) and turning the ingot between each melt to achieve good homogeneity. Then, Al was added to the TiVNb-Mo pre-alloy due to its low melting point (2622 °C for Mo > 2477 °C for Nb > 1910 °C for V > 1670 °C for Ti > 660 °C for Al [30]) and melted under the same conditions. To avoid mass loss during melting all Al small pieces were placed underneath the pre-alloy material. The structural analysis of the as-cast samples was carried out by powder X-ray diffraction (XRD) using a D8 Advance Bruker diffractometer (Cu K_α radiation $\lambda = 1.5406$ Å, Bragg-Brentano geometry).

The microstructure of the as-cast and hydrides was analyzed by scanning electron microscopy (SEM) using a Zeiss Merlin microscope equipped with an EDX (Energy-Dispersive X-ray Spectroscopy) detector from Oxford Instruments and Aztec software. The powder samples were embedded in an epoxy resin and bulk samples were fixed with MCP 70 alloy, then finely polished and finally coated with a 1.5 nm Pd layer. For elemental analysis and chemical mapping, an accelerated electron voltage of 10 keV was used and the element quantification was performed using Al(K), Ti(K), V(K), Nb(L) and Mo (L) signals.

The hydrogen storage properties were determined using a home-made volumetric apparatus equipped with a pressure gauge, calibrated volumes, and set temperature (Sievert's method). The stainless-steel sample holder was filled with small pieces of alloys and sealed using metal gaskets. Prior to the hydrogenation process, an activation procedure was carried out by exposing the sample at 410 °C under dynamic vacuum ($\sim 1 \times 10^{-5}$ mbar) for 12 hrs. Two types of measurements were carried out: absorption kinetics at 25 °C and pressure-composition isotherms (PCIs) under different temperatures. For the absorption kinetics, the sample holder is placed in a water bath under isothermal conditions (25 °C) and the sample is exposed to hydrogen reaching a final equilibrium pressure (P_{eq}) of around 36±1 bar H_2. A resistive furnace was used for the acquisition of PCIs at high temperatures (above 25 °C). The mass of the samples (400-500 mg) was measured carefully before hydrogenation to calculate the storage capacity using the real gas state equation for H_2 obtained from GASPAK version 3.32 software (Cryodata Inc., Horizon Technologies). For acquisition of the PCIs, high purity hydrogen was introduced in small doses step by step until a maximum P_{eq} was reached for the last point around 58 bar, while desorption was performed at 410 °C under dynamic secondary vacuum (~$1x10^{-5}$ mbar) for 12 hrs. The structural characterization of the full deuterides was carried out by *ex situ* powder neutron diffraction (nD with λ=1.28 Å) performed on the D1B beamline at the Institute Laue-Langevin (ILL) at Grenoble (France). The powder sample (~2 g) was place inside a vanadium sample holder and the diffraction patterns were acquired in a scanning range from 0.77 to 128.77 2θ (°) [31].

Finally, thermal desorption spectroscopy (TDS), *in situ* synchrotron X-ray powder diffraction (SR-XRD) and *in situ* nD were performed to determine the hydrogen desorption properties. TDS was carried out using a homemade instrument with a quadrupole mass spectrometer QMS, as described previously [32]. The procedure consisted of loading about 10 mg of the hydride sample into the sample holder, then connecting it to the quadrupole mass spectrometer working under secondary vacuum (~$1x10^{-6}$ mbar) and the desorption profile was recorded by heating the sample at a constant rate of 5 °C/min up to 450 °C. *In situ* SR-XRD experiments during hydrogen desorption at the Cristal beamline of the SOLEIL facility (λ= 0.67156 Å) using quartz capillaries with 1.2 mm diameter were carried out by applying a constant heating ramp with 2 °C/min from

25 °C up to 450 °C under dynamic secondary vacuum. To reduce the X-ray absorbance, the powdered samples were mixed with fumed silica at a mass ratio of 1:2, respectively, and the patterns were recorded every 4 °C in the scanning range from 10 to 60 2θ (°). In addition, *in situ* nD was performed on the D1B beamline (λ=1.28 Å) at the ILL. Deuterated samples were placed inside a silica tube connected to a vacuum equipment (about 10^{-5} mbar). Acquisitions were made with a constant heating rate of 1 °C/min applied up to 450 °C and an acquisition range from 0.77 to 128.8 2θ (°) [31]. Also, the pressure of the desorbed gas during deuterium desorption was recorded.

The lattice parameters of different phases were determined from XRD, *ex situ* SR-XRD, *in situ* SR-XRD and *ex situ* nD patterns using the Rietveld analysis implemented in Fullprof refinement software (Thompson-Cox-Hastings pseudo-Voigt function for the peak shape). Densities were calculated using the mass and volume of the unit cell with the corresponding lattice parameters as determined by XRD and the molar mass of each composition.

For comparison purposes, previous results for the composition $Al_{0.05}(TiVNb)_{0.95}$ will be included or mentioned (*e.g.*, lattice parameter, physicochemical and empirical parameters, capacity, kinetics, thermodynamics, TDS, SR-XRD) [24].

3. RESULTS AND DISCUSSION

3.1 Synthesis and microstructure of the pristine alloys

The novel HEA compositions $Al_{0.05}(TiVNb)_{0.95-x}Mo_x$ (x = 0.05, 0.10) were successfully synthesized by high-temperature arc melting. They crystallize in a single-phase *bcc* type structure ($Im\bar{3}m$) as shown by XRD in Figure 1a. This agrees with previous works on HEAs with the same elements such as $Al_{0.05}TiVNbMo$ [33], AlTiVNbMo [34] and $Al_{0.10}Ti_{0.40}V_{0.20}Nb_{0.20}Mo_{0.10}$ [35]. The *bcc* lattice parameters listed in Table 1 were obtained from Rietveld analysis, demonstrating a good fit for the single-phase solid solutions (Figure SI1 of the supplementary information (SI)). A linear decrease in the lattice parameters is observed with increasing Mo content (Figure 1b), in line with the shift of the diffraction peaks towards higher 2θ angles (°). This trend can be explained by the decrease in the average atomic radius by Mo addition (r_{Ti} = 1.46 Å > r_{Al} = 1.43 Å > r_{Nb} = 1.43 Å > r_{Mo} = 1.36 Å > r_V = 1.32 Å [36]). Similar volume contraction with Mo addition has been reported elsewhere, *e.g.*, for the $Ti_{0.30}V_{0.25}Zr_{0.10}Nb_{0.25}Mo_{0.10}$ [29] and $Ti_{0.20}Zr_{0.20}Hf_{0.20}Mo_{0.40}$ [26]. Additionally, the formation of the *bcc* structure in $Al_{0.05}(TiVNb)_{0.95-x}Mo_x$ (x = 0.05, 0.10) can be explained by the stabilizing effect of Mo, Nb and V on the *bcc*-phase when alloyed with Ti (*hcp*-Ti at RT and *bcc*-Ti in the molten state above 832 °C) as reported for some traditional *bcc* alloys [25,37] and HEAs [26]. Also, Al acts as a *bcc* stabilizer as was earlier proven for similar compositions Al_xNbTiMoV [33].

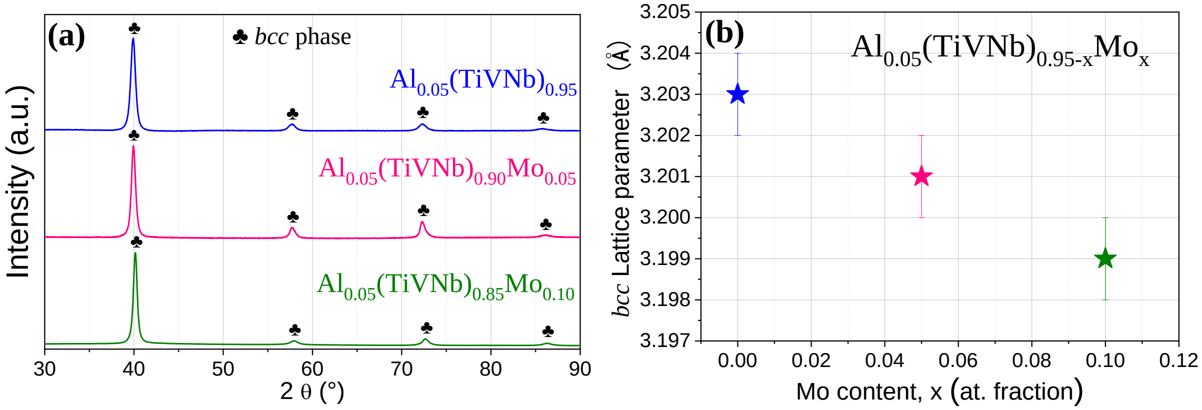

Figure 1. (a) XRD patterns (λ = 1.5406Å) of $Al_{0.05}(TiVNb)_{0.95-x}Mo_x$ (x = 0 [24], 0.05, 0.10). (b) *bcc* lattice parameters as a function of Mo content.

Empirical parameters for predicting HEA phase stability, such as lattice distortion (δ) and VEC, were calculated as described by Miracle and Senkov [36] and are listed in Table 1 together with the experimental values of density (g/cm^3) and *bcc* lattice parameters. All compositions have nearly identical values (δ and VEC) in the range where single-phase *bcc* solid solutions are expected (δ

< 6.6% [11] and VEC < 6.87 [13]), as experimentally corroborated by the XRD patterns. The bulk density parameter (ρ) increases slightly from 6.3 to 6.6 g/cm^3 with Mo content due to its heavier weight compared to the other elements. Since their density is below 7.1 g/cm^3, they can be considered as "lightweight" refractory HEAs based on the criteria defined elsewhere [38] as well as for the equimolar AlTiVNbMo [34] and for $Ti_{40}Al_{10}V_{20}Nb_{20}Mo_{10}$[35].

Table 1. Physicochemical parameters (molar mass and bulk density), empirical parameters (δ and VEC) and lattice parameters of the as-cast $Al_{0.05}(TiVNb)_{0.95-x}$ (x=0 [24], 0.05, 0.10) alloys.

Composition	Molar mass (g/mol)	ρ (g/cm^3)	δ (%)	VEC	Lattice parameter (Å)	Reference
$Al_{0.05}(TiVNb)_{0.95}$	62.1	6.3	4.3	4.6	3.203 (1)	[24]
$Al_{0.05}(TiVNb)_{0.90}Mo_{0.05}$	63.7	6.4	4.3	4.7	3.201 (1)	Present work
$Al_{0.05}(TiVNb)_{0.85}Mo_{0.10}$	65.3	6.6	4.2	4.7	3.199 (1)	Present work

Chemical mapping and elemental analysis of the microstructure of the as-cast materials analyzed by SEM-EDX, are shown in Figure 2 and Table 2, respectively. The dendrites with high brightness intensity correlate to the presence of Nb and Mo, while the interdendrite zones are mainly dominated by Al/Ti/V. Despite this microstructure, Table 2 shows that the average chemical composition is in good agreement with the nominal one. These small chemical modulations are common in HEAs and have been attributed to the alloying element partitioning in the solid/liquid phase interface during the solidification process. Slow cooling rates typical for arc melting mostly favor the formation of dendrites and the elements that enrich these dendritic areas are the ones with the highest melting points [33,39,40]. The highest melting points of the constituent elements in these compositions are Mo and Nb (2622 °C for Mo > 2477 °C for Nb > 1910 °C for V > 1670 °C for Ti > 660 °C for Al [30]), in line with their tendency to be found in dendritic areas. Similarly, $Al_xNbTiMoV$ has dendrites enriched with Mo/Nb due to their higher melting points, while the interdendrites are enriched with Al/Ti due to their more negative enthalpy of mixing and lower melting points [33]. Therefore, XRD and SEM-EDX confirm the formation of a single-phase *bcc* solid solution for $Al_{0.05}(TiVNb)_{0.95-x}Mo_x$ (x=0.05, 0.10) with chemical composition close to the nominal one.

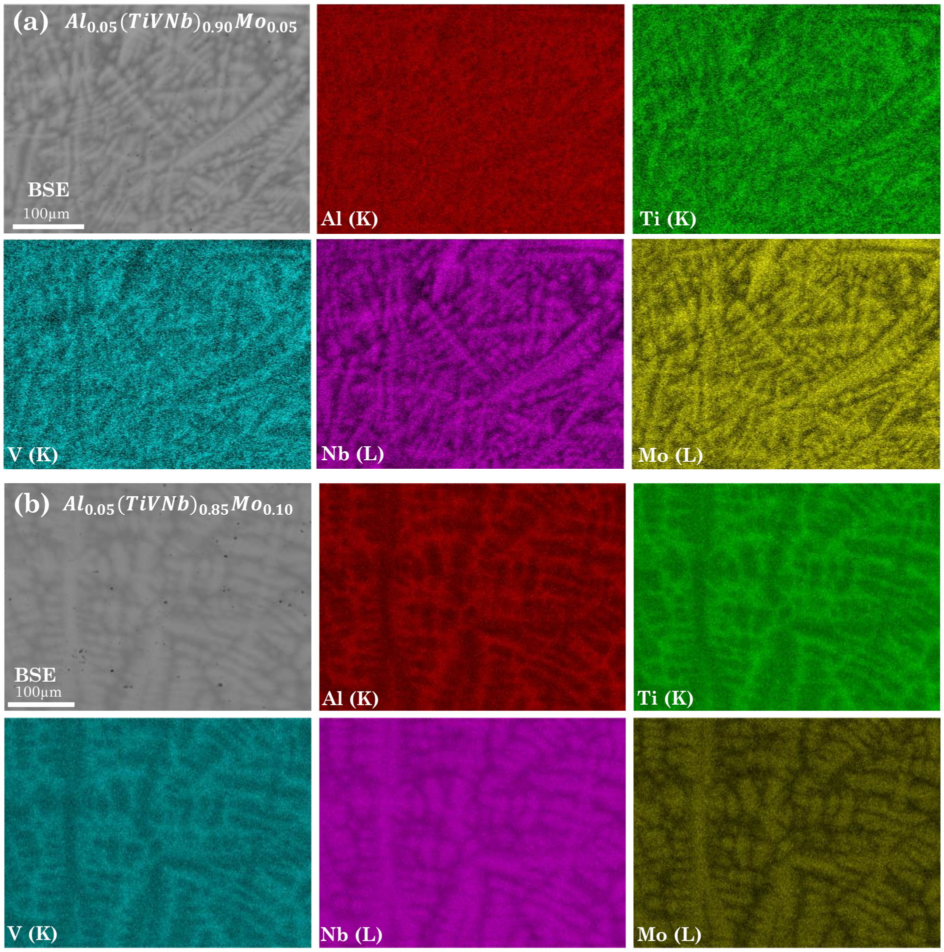

Figure 2. (a) XRD SEM-EDX chemical mapping of the as-cast (a) $Al_{0.05}(TiVNb)_{0.90}Mo_{0.05}$ and (b) $Al_{0.05}(TiVNb)_{0.85}Mo_{0.10}$.

Table 2. EDX elemental analysis of the as-cast $Al_{0.05}(TiVNb)_{0.95-x}Mo_x$ (x=0.05, 0.10).

Composition	Element	Nominal (at. %)	Overall average (at. %)	Dendritic zone (at. %)	Interdendritic zone (at. %)
$Al_{0.05}(TiVNb)_{0.90}Mo_{0.05}$	Al (K)	5	4.9 (0.3)	4.8 (0.3)	4.9 (0.2)
	Ti (K)	30	29.8 (0.9)	29.1 (0.7)	30 (0.9)
	V (K)	30	29.6 (0.9)	29 (1.2)	29.7 (0.8)
	Nb (L)	30	31.1 (1.4)	31.5 (1.8)	31.1 (1.3)
	Mo (L)	5	4.6 (0.6)	5.6 (0.3)	4.3 (0.4)
$Al_{0.05}(TiVNb)_{0.85}Mo_{0.10}$	Al (K)	5	4.1 (0.4)	4.1 (0.3)	4.1 (0.4)
	Ti (K)	28.4	29 (0.7)	28.8 (0.5)	29.1 (0.7)
	V (K)	28.3	28.8 (0.7)	28.1 (0.6)	29 (0.6)
	Nb (L)	28.3	28.5 (0.6)	28.7 (0.5)	28.4 (0.6)
	Mo (L)	10	9.6 (0.5)	10.3 (0.2)	9.4 (0.4)

3.2 Hydrogen absorption kinetics and hydride structure

Prior to hydrogenation, the samples were activated to remove the surface contamination of alloys, which is often passivated with different contaminants [41]. The hydrogenation of the activated compositions $Al_{0.05}(TiVNb)_{0.95-x}Mo_x$ (x=0.05, 0.10) was carried out in a single aliquot of hydrogen under 25 °C with a final equilibrium pressure around 36±1 bar. The kinetics (Figure 3) showed a rapid absorption of hydrogen with a maximum capacity of 1.78 and 1.79 H/M for x = 0.05, 0.10, respectively, which is slightly smaller but very close to 1.8 H/M for x = 0 ($Al_{0.05}(TiVNb)_{0.95}$) [24]. Overall, the Mo has a positive impact on the kinetics decreasing the time to reach maximum uptake, especially for the highest Mo content.

The structural analysis of the hydrides is displayed in Figure SI2 with the respective Rietveld analysis, showing the formation of *fcc* dihydride for $Al_{0.05}(TiVNb)_{0.90}Mo_{0.05}H_{1.78}$ (Figure SI2a) with a lattice parameter of 4.408 (1) Å (Table 3). On the contrary, $Al_{0.05}(TiVNb)_{0.85}Mo_{0.10}H_{1.79}$ (Figure SI2b) displays a mixture of a *fcc* dihydride with a lattice parameter of 4.395 (1) Å (Table 3) and a small amount of *bcc* phase (15% phase fraction, Table 3) that could be considered as a monohydride with higher lattice parameter (3.335(1) Å, Table 3) than the as-cast material (Table 1).

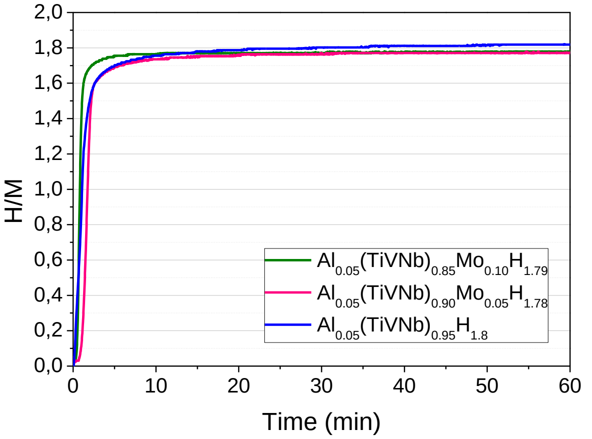

Figure 3. Kinetics of absorption at 25 °C under 36±1 bar of H_2 for $Al_{0.05}(TiVNb)_{0.95-x}Mo_x$ (x=0 [24], 0.05, 0.10).

The gravimetric hydrogen storage capacities for $Al_{0.05}(TiVNb)_{0.95-x}Mo_x$ (x=0.05, 0.10) (2.79 wt.% and 2.75 wt.%, respectively) are slightly smaller than 2.9 wt.% obtained for $Al_{0.05}(TiVNb)_{0.95}$ [24] due to the addition of Mo which is the heaviest element among all components. However, these values are close to the highest capacities reported for lightweight HEAs/MPEAs materials such as, $Ti_{0.30}V_{0.25}Zr_{0.10}Nb_{0.25}Al_{0.10}$ (2.6 wt.%) [23], $Al_{0.05}(TiVNb)_{0.95}$ (2.96 wt.%) [24], $Ti_{0.30}V_{0.25}Zr_{0.10}Nb_{0.25}Mg_{0.10}$ (2.7 wt.%) [22], and $Mg_{35}Al_{15}Ti_{25}V_{10}Zn_{15}$ (2.5 wt.%) [21]. Moreover, the compositions reported in this work have higher gravimetric capacity that other refractory HEAs such as, $Ti_{0.325}V_{0.275}Zr_{0.125}Nb_{0.275}$ (2.5 wt.%) [28], TiVZrNbMo (2.3 wt.%) [42], $TiHfZrNb_{1-x}V_{1+x}$ (≃2 wt.%) [43] and $Ti_{0.30}V_{0.25}Zr_{0.10}Nb_{0.25}Ta_{0.10}$ (2.5 wt.%) [44]. An increase in gravimetric capacity by Mo addition has also been reported in $Ti_{0.30}V_{0.25}Zr_{0.10}Nb_{0.25}Mo_{0.10}$ (2.8 wt. %) [29] and in $Ti_{0.20}Zr_{0.20}Hf_{0.20}Mo_{0.10}Nb_{0.30}$ (1.54 wt.%) [26], while higher Mo content typically decreases the gravimetric capacity, as observed in $Ti_{0.20}Zr_{0.20}Hf_{0.20}Mo_{0.40}$ (0.92 wt.%) [26] and in equimolar TiZrHfMoNb (1.18 wt.%) [45]. In our work, the gravimetric capacity declines as Mo content increases because it is not fully hydrogenated under the present conditions *i.e*, under around 36±1 at room temperature (as shown in Figure SI2b).

Subsequently, the structural properties of the deuterides were analyzed by *ex situ* neutron diffraction (nD) for $Al_{0.05}(TiVNb)_{0.90}Mo_{0.05}D_{1.77}$ and $Al_{0.05}(TiVNb)_{0.85}Mo_{0.10}D_{1.79}$ in Figures 4a and b together with their respective Rietveld fitting. The use of deuterium isotope instead of hydrogen for the structural analysis by nD is intended to reduce the hydrogen incoherent neutron scattering cross section and to avoid a high level of background [46]. Moreover, due to its relatively large coherent scattering length (+ 6.67 fm) as compared to the present alloys, deuterium can be localized in the interstitial sites of the hydride phase by nD. For comparison, the nD pattern for $Al_{0.05}(TiVNb)_{0.95}D_{1.81}$ is plotted in Figure SI3. The analysis of nD diffraction patterns revels a good fit for a single-phase *fcc* (CaF_2-type, $Fm\bar{3}m$) with a decreasing lattice parameter (from a_{fcc}=4.371(1) Å to a_{fcc}=4.358(1) Å) with increasing Mo content (Table 3). Deuterium atoms were, however, located in the tetrahedral interstitial sites of the *fcc* structure, in agreement with previous studies on TiVNb [17], $Ti_{0.30}V_{0.25}Zr_{0.10}Nb_{0.25}Ta_{0.10}$ [44], and TiZrHfMoNb [45] where the hydrogenation process induces a similar phase transformation from an initial *bcc* lattice to the *fcc* dihydride phase. The *bcc* deuterated phase in $Al_{0.05}(TiVNb)_{0.85}Mo_{0.10}D_{1.79}$ is not visible by nD but can be noticed in the XRD pattern as shown in Figure SI2b. This is due to the small coherent neutron scattering cross section of the metallic constituents and possibly a disorder of deuterium occupancy in the intermediate *bcc* phase.

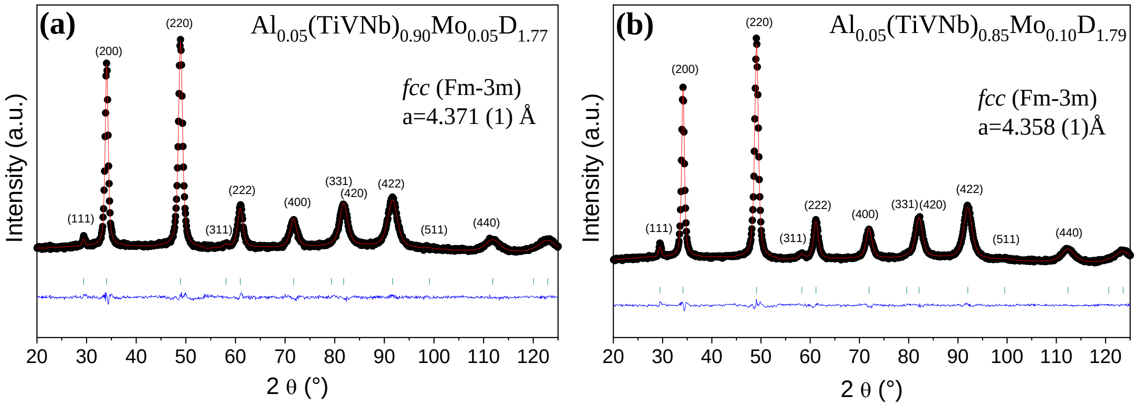

Figure 4. *Ex situ* powder nD patterns (D1B at ILL, λ=1.28 Å) of fully deuterated samples, corresponding Rietveld refinement analysis and lattice parameter, (a) $Al_{0.05}(TiVNb)_{0.90}Mo_{0.05}D_{1.77}$ and (b) $Al_{0.05}(TiVNb)_{0.85}Mo_{0.10}D_{1.79}$.

Table 3. Structural parameters of the *fcc* deuterides as determined by Rietveld analysis of *ex situ* nD (λ=1.28 Å) and *fcc* hydrides obtained by Rietveld analysis of XRD.

Composition	Form	Phase	Space group	Lattice parameter (Å)	Phase fraction (%)	Reference
$Al_{0.05}(TiVNb)_{0.95}H_{1.84}$	hydride	*fcc*	*Fm-3m*	4.418 (1)	100	[24]
$Al_{0.05}(TiVNb)_{0.95}D_{1.81}$	deuteride	*fcc*	*Fm-3m*	4.383 (1)	100	Present work
$Al_{0.05}(TiVNb)_{0.90}Mo_{0.05}H_{1.78}$	hydride	*fcc*	*Fm-3m*	4.408 (1)	100	Present work
$Al_{0.05}(TiVNb)_{0.90}Mo_{0.05}D_{1.77}$	deuteride	*fcc*	*Fm-3m*	4.371 (1)	100	Present work
$Al_{0.05}(TiVNb)_{0.85}Mo_{0.10}H_{1.79}$	hydride	*fcc*	*Fm-3m*	4.395 (1)	85	Present work
		bcc	*Im-3m*	3.335 (1)	15	
$Al_{0.05}(TiVNb)_{0.85}Mo_{0.10}D_{1.79}$	deuteride	*fcc*	*Fm-3m*	4.358 (1)	100	Present work

3.3 Data-driven models of hydride reaction enthalpy

Trained on experimental metal hydride thermodynamic data and accompanied by experimental validation, data-driven models can qualitatively and quantitatively predict the effects of alloy composition tuning on hydride reaction enthalpies [16,47–49]. Because the accuracy of such methods are typically improved by including more training data, we created the ML-ready HydPARK Zenodo repository [50] which we continually update as more experimental data becomes available. For this study we released v0.0.5 of the ML-ready HydPARK database, which augments v0.0.4 with the comprehensive AB_2 metal hydride thermodynamic data recently presented in Ref. [51]. Gradient boosting tree models were trained to predict the enthalpy of the hydriding reaction, ΔH, using the identical strategy described in Ref. [16], with scripts to reproduce them provided here (https://github.com/mwitman1/HEAhydrideMLv2). Figure 5 shows the K=10-fold cross-validation test set predictions for ΔH, (left column), the training data distribution and MAE of these test set predictions as a function of true experimental value (middle column), and the SHapely Addititve Prediction (SHAP) values (right column) for models trained on v0.0.4 of the database (top row) vs. v0.0.5 of the database (bottom row). The test set MAE, averaged across all K-folds, decreases notably between v0.0.4 (5.4 kJ/mol H_2) and v0.0.5 (4.2 kJ/mol H_2). Figure 5 (middle column) reveals that while the additional ~300 hydrides added in v0.0.5 do not substantially improve the data imbalance of the training set, v0.0.5 does improve the representation of low ΔH hydrides in the training data. Therefore, the bulk of this MAE reduction occurs in the prediction of low ΔH hydrides. Finally, the SHAP analyses in Figure 5 (right column) are qualitatively consistent between v0.0.4 and v0.0.5 models. Denoting a composition-weighted mean property as $\bar{p} = \sum x_i p_i$ (x_i = composition fraction of element i and p_i = elemental property of i), the v0.0.5 model's predictions retain the largest feature dependence on the mean volume per atom ($p = \bar{v}_{pa}$).

Secondary structure-property relationships depending on space group number ($p = \overline{\mathrm{SG}\#}$), the Pauling electronegativity ($p = \bar{\chi}$), binary hydride formation enthalpy ($p = \Delta\bar{H}_b$), and melting temperature ($p = \bar{T}_m$) remain similar. This indicates that the model-elucidated composition-property relationships that determine hydriding thermodynamics have not undergone significant qualitative change with the additional training data, but have been quantitatively refined. These models can subsequently be used to predict the destabilizing effect of Mo addition on the $Al_{0.05}(TiVNb)_{0.95}$ (Table 4).

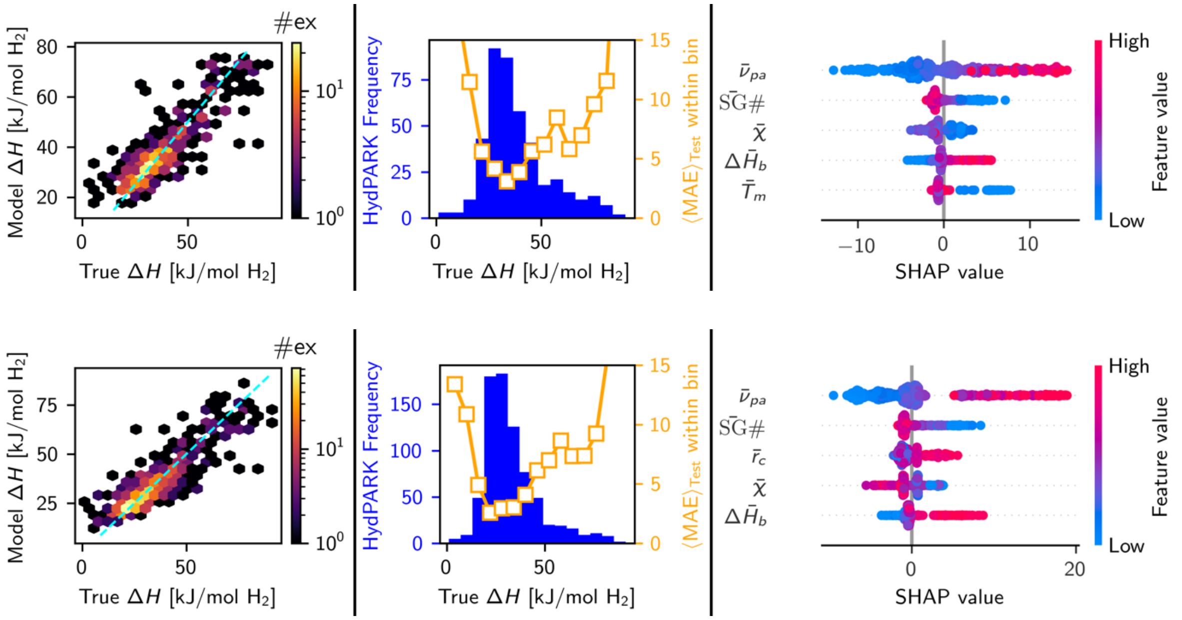

Figure 5. Validation of the hydride reaction enthalpy model trained on v0.0.4 (top row) vs. v0.0.5 (bottom row) of the ML-ready HydPARK database. The K=10-fold cross-validation test set predictions for predicting ΔH (left column), the MAE of these test set predictions as a function of the true experimental value (middle column), and the SHapely Additive Prediction (SHAP) values (right column) are shown.

3.4 Thermodynamics of hydrogen absorption and desorption

The hydrogen absorption PCI curves were constructed using a Sievert's apparatus at different temperatures for the compositions $Al_{0.05}(TiVNb)_{0.90}Mo_{0.05}$ (Figure 6a) and $Al_{0.05}(TiVNb)_{0.85}Mo_{0.10}$ (Figure 6b). The absorption PCIs for $Al_{0.05}(TiVNb)_{0.95}$ have been previously reported [24] and the thermodynamic parameters obtained (ΔH_{abs} and ΔS_{abs}) will be included in the discussion. Both new compositions show a two-step reaction with hydrogen : the first one forms a monohydride phase with maximum 0.9 H/M at equilibrium pressures below the detection limits of the pressure transducer ($<10^{-2}$ bar), while the second reaction is related to the formation of the dihydride phase at higher equilibrium pressure that increases as a function of the temperature. These results are in good agreement with the observed two-step transition (first-order phase transition), from *bcc* ↔ *bcc* monohydride ↔ *fcc* dihydride, as shown for both TiVNb and $Al_{0.05}(TiVNb)_{0.95}$ [24], but also for other conventional *bcc* alloys [52–54] and HEAs [18,24,55–57]. The maximum capacity values from the PCIs at 25 °C for $Al_{0.05}(TiVNb)_{0.90}Mo_{0.05}$ and $Al_{0.05}(TiVNb)_{0.85}Mo_{0.10}$ are 1.78 H/M (2.79 wt.%) and 1.79 H/M (2.75 wt.%), respectively; these values agree well with the absorption kinetics experiments.

The addition of Al/Mo in our system reduces the slope of the plateaus observed for the ternary TiVNb alloy [56] which affords the appropriate application of van't Hoff approach. Thermodynamic values for the second phase transition were obtained (Figure 6c) and are compared with those of $Al_{0.05}(TiVNb)_{0.95}$ [24] and other similar compositions based on TiVNb in Table 4. The addition of 5-10 at.% Al in the TiVNb system destabilizes the hydride phase, while much larger amounts of Cr must be added to TiVNb (25-35 at.% Cr [58], [59]) to achieve the same effect. Use of Al/Cr in equal proportions in $(TiVNb)_{100-x}(CrAl)_x$ can even further destabilize the dihydride phase [27]. Here we have demonstrated that the addition of small amounts of Mo (5-10 at.%) can more substantially destabilize the hydride formation, with one of the smallest values reported for the enthalpy of hydride formation for $Al_{0.05}(TiVNb)_{0.85}Mo_{0.10}$ (ΔH_{abs}= -37(±1) kJ/mol H_2). The trend in hydride destabilization as a function of Mo addition is qualitatively and quantitatively captured by gradient boosting tree ML model predictions (Figure 6d), once again confirming its utility for *a priori*, rational design of HEA hydrides with targeted thermodynamic properties [16,47–49].

The well-known Miedema rule of reversed stability predicts that less stable alloys form more stable hydrides and *vice versa* [60]. Previous reports put forward that the addition of Al in refractory HEAs stabilizes the *bcc* lattice and inhibits the formation of intermetallic secondary phases [33,61,62]. According to Hume-Rothery rules, Mo is also considered an element promoting *bcc* phase in HEAs [63]. Consequently, it might be considered that the present compositions have high *bcc* phase stability which may be responsible for the less stable hydrides, according to Miedema rule [64,65]. Applying the van't Hoff equation ($\ln P_{eq} = -\Delta H_0/RT + \Delta S_0/R$) to the PCI data shown in Figure SI4a, b, we obtained the corresponding van't Hoff plot for desorption (Figure SI4c). For $Al_{0.05}(TiVNb)_{0.90}Mo_{0.05}$ we obtain ΔH_{des} = 58(±4.5) kJ/mol H_2 and ΔS_{des} = 152(±12) J/(K mol H_2), while for $Al_{0.05}(TiVNb)_{0.85}Mo_{0.10}$ we obtain ΔH_{des} = 47(±1.3) kJ/mol H_2 and ΔS_{des} = 137(±4) J/K mol H_2. Moreover, the experimental entropy loss values are close to the expected entropy of free H_2 gas (~130 J/(K mol H_2)).

Along with Miedema rule of reversed stability, other possible explanations may be invoked to clarify the observed thermodynamic destabilization such as, steric effects due to reduced lattice parameters by Mo addition or repulsive interactions between H and both non-hydride forming elements, Al and Mo [66].

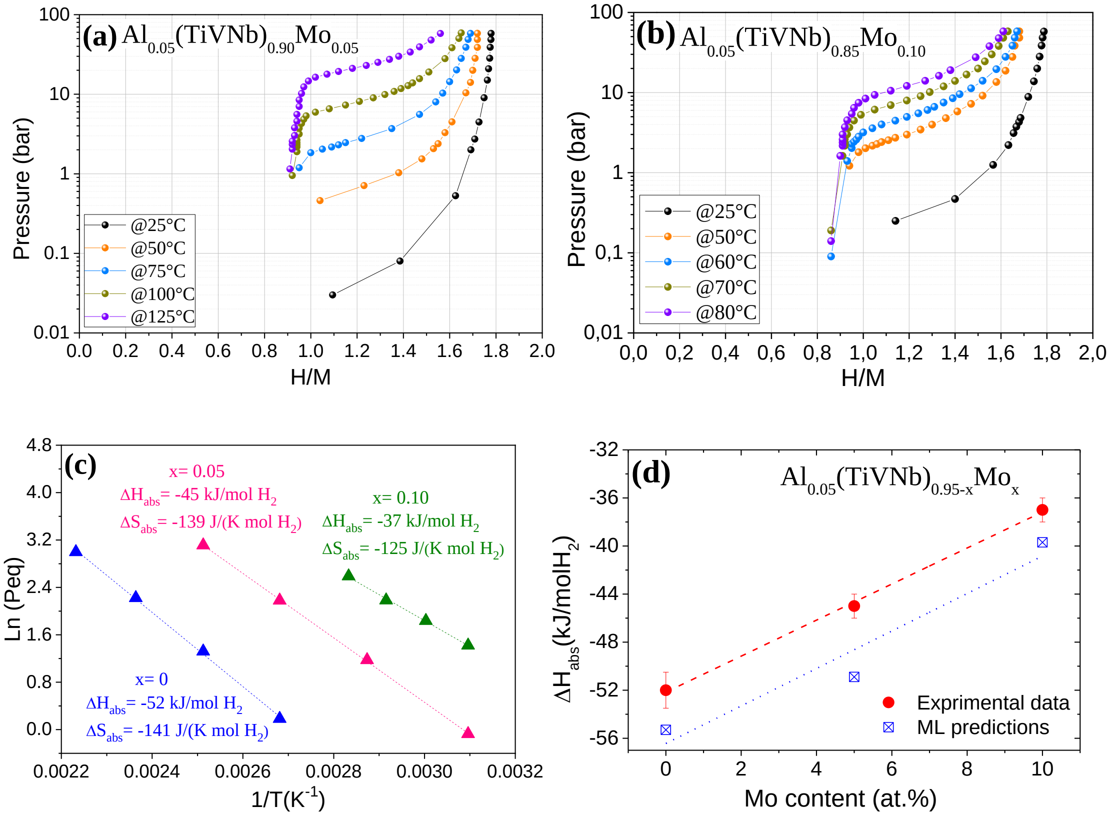

Figure 6. PCIs at different temperatures of (a) $Al_{0.05}(TiVNb)_{0.90}Mo_{0.05}$ and (b) $Al_{0.05}(TiVNb)_{0.85}Mo_{0.10}$. (c) van't Hoff plots for $Al_{0.05}(TiVNb)_{0.95\text{-}x}Mo_x$ (x=0,0.05,0.10). (d) Comparison of ΔH_{abs} between experimental data and predicted data from the ML model for $Al_5(TiVNb)_{95\text{-}x}Mo_x$ (x=0, 5, 10 at. %).

Table 4. Thermodynamic properties of dihydride formation for $Al_{0.05}(TiVNb)_{0.90}Mo_{0.05}$ and $Al_{0.05}(TiVNb)_{0.85}Mo_{0.10}$ together with compositions (TiVNb-base) with measurable data for comparison. For the present work: experimental data (*exp.*) and machine learning predicted data (ML).

Composition	ΔH_{abs} (kJ/mol H_2)	ΔS_{abs} (J/(K mol H_2))	Reference
$Al_{0.10}(\mathbf{TiVNb})_{0.80}Cr_{0.10}$	-34	-130	[27]
$Al_{0.05}(\mathbf{TiVNb})_{0.85}Mo_{0.10}$	-37 (±1) *exp.*, -39.7 ML	-125 (±3)	Present work
$(\mathbf{TiVNb})_{0.75}Cr_{0.35}$	-39	-134	[59]
$Al_{0.05}(\mathbf{TiVNb})_{0.90}Mo_{0.05}$	-45 (±1) *exp.*, -50.90 ML	-139 (±1.5)	Present work
$Al_{0.10}(\mathbf{TiVNb})_{0.90}$	-48.6	-154	[56]
$Al_{0.05}(\mathbf{TiVNb})_{0.90}Cr_{0.05}$	-49	-139	[27]
$\mathbf{TiV}Cr\mathbf{Nb}$	-51.6	-129.3	[58]
$Al_{0.05}(\mathbf{TiVNb})_{0.95}$	-52 *exp.*, -55.3 ML	-141	[24]
$\mathbf{TiV_{0.5}}Zr\mathbf{Nb}Hf$	-59.1	-87.4	[17]
$\mathbf{TiV}Zr\mathbf{Nb}Hf$	-61.8	-88	[17]
$\mathbf{TiVNb}$	-67	-157	[56]
$(\mathbf{TiVNb})_{0.85}Cr_{0.15}$	-67	-172	[67]
$\mathbf{TiV}Zr\mathbf{Nb}$	-67.6	-90.3	[17]
$\mathbf{Ti_{0.30}V_{0.25}}Cr_{0.10}Zr_{0.10}\mathbf{Nb_{0.25}}$	-75	-161	[55]

3.5 Hydrogen desorption-induced phase change characterization

To investigate the phase transformation during desorption, the deuterides $Al_{0.05}(TiVNb)_{0.95}D_{1.81}$, $Al_{0.05}(TiVNb)_{0.90}Mo_{0.05}D_{1.77}$ and $Al_{0.05}(TiVNb)_{0.85}Mo_{0.10}D_{1.79}$ were prepared. *In situ* neutron thermo-diffractogram during deuterium desorption along with the vacuum pressure readings are shown in Figure SI5 and Figure 7a-b, respectively. The *in situ* nD of $Al_{0.05}(TiVNb)_{0.90}Mo_{0.05}D_{1.77}$

(Figure 7a) shows the stability of the initial *fcc* phase (marked with ♥) up to around 97 °C which corresponds to the onset temperature (T_{onset}) in the pressure reading profile. At about 129 °C the intensity of the diffraction peaks starts to decrease, and we observe the first event in the desorption profile. Above 129 °C, the *bcc* phase (marked with ♣) is noticed with a weak intensity due to low neutron scattering cross-section of the alloy without deuterium, as previously reported [17]. At 217 °C, the *fcc* signal fades and a second desorption event is observed in the pressure reading. Above 217 °C only the presence of the desorbed *bcc* phase is visible which shifts towards higher 2θ (°) due to the shrinking of the lattice upon desorption. Likewise, the *in situ* thermo-diffractogram of $Al_{0.05}(TiVNb)_{0.85}Mo_{0.10}D_{1.79}$ in Figure 7b shows the same qualitative structural evolution upon deuterium desorption. At 127 °C the *bcc* desorbed phase (♣) appears and around 181 °C the *fcc* phase (♥) completely disappears indicating the second event in the pressure reading profile. This reveals that the addition of Mo shifts the desorption events to lower temperatures compared to $Al_{0.05}(TiVNb)_{0.95}D_{1.81}$ which shows a T_{onset} at 107 °C and the disappearance of the *fcc* phase at about 227 °C (Figure SI5). The results are in good agreement with the previously demonstrated thermodynamic destabilization of the dihydride phase with increasing Mo content. However, we only observe a phase transition from the *fcc* phase to the fully-desorbed *bcc* alloy phase. The deuterated *bcc* phase (∼1 D/M) cannot be detected by *in situ* nD due to low neutron scattering cross-section of the alloy and possible deuterium disorder as hypothesized above. Thus, the thermal evolution of *bcc*-phase could not be qualitatively determined y *in situ* nD.

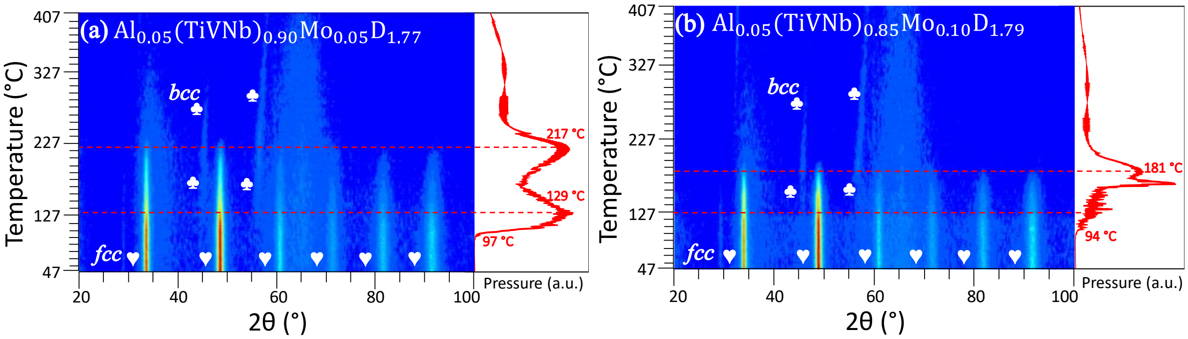

Figure 7. *In situ* nD thermo-diffractograms (λ= 1.28 Å) of fully deuterated samples (a) $Al_{0.05}(TiVNb)_{0.90}Mo_{0.05}D_{1.77}$ and (b) $Al_{0.05}(TiVNb)_{0.85}Mo_{0.10}D_{1.79}$. The heating rate is 1 °C/min.

For additional phase transition characterization, full hydrides of $Al_{0.05}(TiVNb)_{0.90}Mo_{0.05}$ and $Al_{0.05}(TiVNb)_{0.85}Mo_{0.10}$ were investigated by TDS and *in situ* SR-XRD. First, TDS analysis shows a shift of T_{onset} with increasing Mo content from 174 °C to 116 °C, respectively (Figure SI6a and b), confirming that Mo at 10 at. % drastically decreases the desorption onset temperature. The *bcc* ↔ *fcc* structural reversibility is an important feature, therefore the crystalline structure after desorption performed by TDS was analyzed by XRD. The XRD patterns along with the Rietveld refinement analysis confirmed the complete desorption and recovery of the single *bcc*-phase (Figures SI7a and SI7b). The lattice parameters after desorption of $Al_{0.05}(TiVNb)_{0.90}Mo_{0.05}$ and $Al_{0.05}(TiVNb)_{0.85}Mo_{0.10}$ are a_{bcc}=3.203(1) Å and a_{bcc}=3.195(1) Å, respectively. Consequently, these lattice parameters are close to those obtained from the as-cast materials (Table 1), confirming reversible hydrogen uptake and release.

Additional *in situ* SR-XRD experiments (heating ramp of 2 °C/min) were performed starting from full hydrides to better study the phase transformations and try to identify the different desorption steps. The thermo-diffractograms of $Al_{0.05}(TiVNb)_{0.90}Mo_{0.05}H_{1.78}$ and $Al_{0.05}(TiVNb)_{0.85}Mo_{0.10}H_{1.79}$ are shown in Figures 8a and 8b, respectively. The lattice parameters and phase fractions calculated from Rietveld refinements of *in situ* SR-XRD patterns as function of temperature are shown in the middle and on the right of Figures 8a and 8b, respectively, and also listed in Table SI1. The SR-XRD patterns of the initial dihydrides and final phases recorded at 25 °C are shown in Figure SI8a-d.

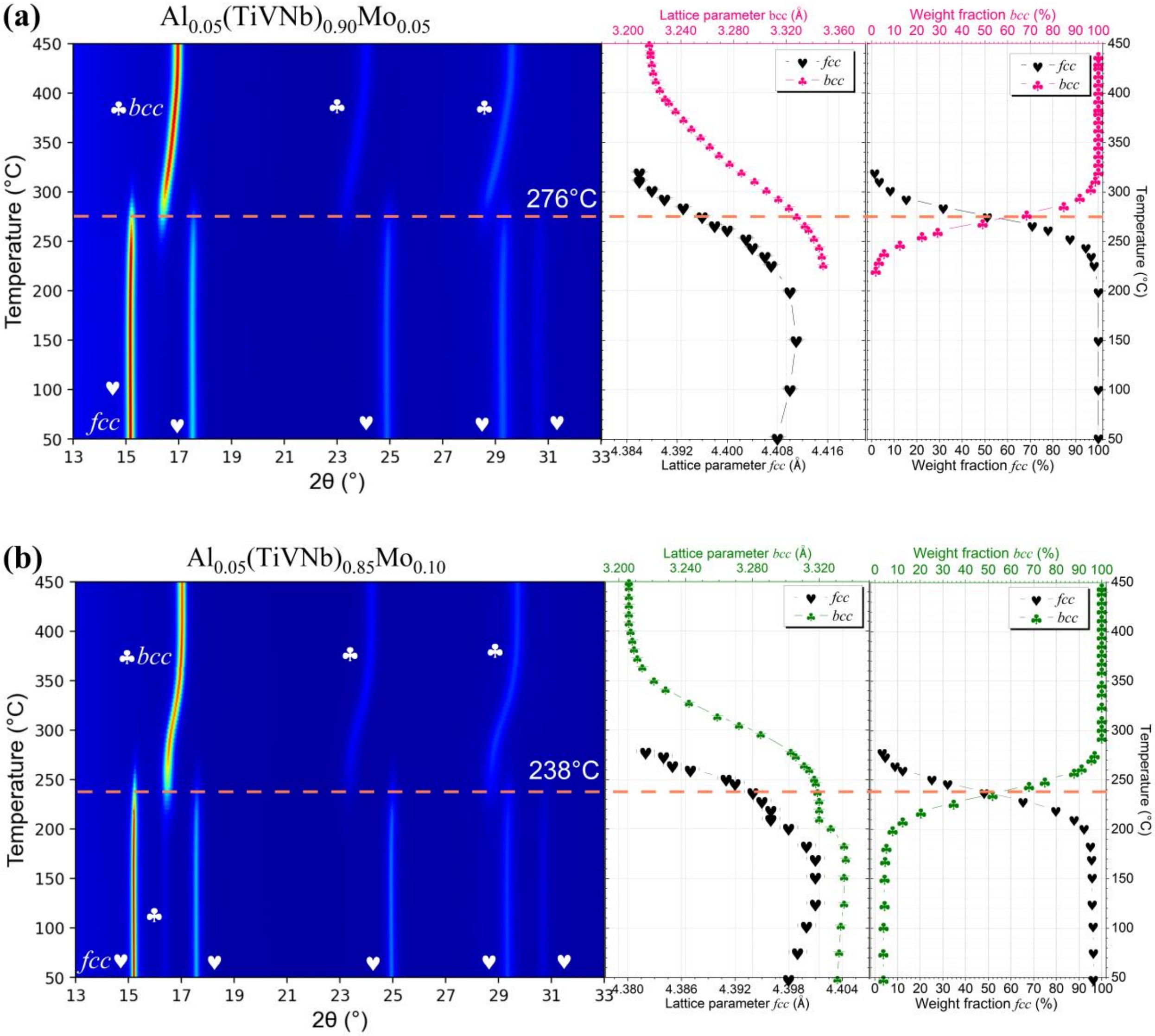

Figure 8. *In situ* SR-XRD thermo-diffractograms (λ= 0.67156 Å) of the hydrides (a) Al$_{0.05}$(TiVNb)$_{0.90}$Mo$_{0.05}$H$_{1.78}$ and (b) Al$_{0.05}$(TiVNb)$_{0.85}$Mo$_{0.10}$H$_{1.79}$ during desorption from 50 °C to 450 °C (2 °C/min) under secondary vacuum. Thermal evolution from *fcc* to *bcc* lattice parameters and thermal evolution of the phase fractions of the hydrides (on the right). Evolution of *fcc* phase (marked with ♥) towards *bcc* (marked with♣).

The $Al_{0.05}(TiVNb)_{0.90}Mo_{0.05}H_{1.78}$ initial *fcc* phase (marked with ♥, Figure 8a) is stable in the range of 25 - 200 °C with a lattice parameter around 4.410(1) Å (Table SI1). Above this temperature the *fcc* phase starts to desorb hydrogen and the formation of the *bcc* phase is observed (marked with ♣, Figure 8a). This temperature is near the T_{onset} from the TDS profile (174 °C, Figure SI6a) with a small difference due to the different experimental conditions (heating ramps, vacuum environments). Notably, there is a coexistence of the *fcc* and the recovered *bcc* phases from 230 °C up to around 300 °C, with the lattice parameters of both phases steadily decreasing (Table SI1, Figure 8a on the right). From 320 °C the *fcc* phase vanishes and only the *bcc* component is present with a lattice parameter progressively decreasing from 3.277(1) Å to 3.216(1) Å at 450 °C (Table SI1, Figure 8a on the right). The lattice parameter of the *bcc* phase at 450 °C (3.216(1) Å) is larger than at 25 °C (3.206(1) Å, Table SI1) which can be attributed to thermal expansion. Upon cooling to 25 °C, this lattice parameter of the *bcc* desorbed phase (3.206(1) Å) is close that of the as-cast material (3.201(1) Å, Table 1). These results suggest complete desorption and reversibility of the alloy. The constant decrease of the *bcc* lattice parameter above 230 °C indicates that high temperatures are needed to desorb hydrogen from the monohydride phase.

Similarly, the *in situ* SR-XRD profile from $Al_{0.05}(TiVNb)_{0.85}Mo_{0.10}\ H_{1.79}$ showed a progressive recovery of the *bcc* phase with the disappearance of the *fcc* component. Initially, the dihydride *fcc* phase (marked with ♥, Figure 8b) coexists with a minor *bcc* phase (marked with ♣, Figure 8b). In the temperature range 25 – 170 °C, a slight increase of both lattice parameters is observed due to thermal expansion from a_{fcc} = 4.398(1) to a_{fcc} = 4.401(1) Å, and from a_{bcc} = 3.330(1) to a_{bcc}=3.336(1) Å (Figure 8b on the right and Table SI1), respectively. At 180 °C, both phases start to desorb hydrogen with a decrease in the lattice parameter values. From 200 °C to 229 °C, the lattice parameters remain constant (Figure 8b on the right and Table SI1). However, the *fcc* phase fraction decreases (from 88 to 65%) and the *bcc* phase fraction increases (from 12 to 35%). This corresponds to the phase transition during temperature increase with lattice shrinkage due to hydrogen desorption and thermal expansion occurring simultaneously in this temperature range (Figure 8b on the right, Table SI1). The two phases then coexist in almost equal proportions until a temperature of 238 °C is reached. Above this temperature, the *fcc* fraction decreases significantly while *bcc* fraction increases until 280 °C (Figure 8b on the right and Table SI1). A decrease in both lattice parameters from a_{fcc}=4.394(1) to a_{fcc} = 4.382(1) Å and from a_{bcc} = 3.319(1) to a_{bcc} = 3.303(1) Å is also observed (Figure 8b on the right and Table SI1). Above 300 °C, only the *bcc* phase is present, with a sharp decrease in the lattice parameter from 3.285(1) at 300 °C to 3.221(1) Å at 350 °C (Figure 8b on the right and Table SI1). In Figure 8b a more pronounced shift of the *bcc* phase towards higher 2θ (°) can be observed. Finally, from 364 °C up to 450 °C there is a smooth decline of the lattice parameters from 3.214(1) to 3.206(1) Å (Figure 8b on the right and Table SI1). The *bcc* lattice parameter at 450 °C (3.206(1) Å, Table SI1) is larger than the as-cast (3.199(1) Å, Table 1) due to thermal expansion, while the lattice parameter at 25 °C (3.196(1) Å, Table SI1) is close to that of the as-cast material (3.199(1) Å, Table 1). In other words, complete desorption has been achieved under *in situ* SR-XRD conditions with a complete recovery of the *bcc* phase. However, only one phase transition from *fcc*/*fcc*+*bcc* to *bcc* phase is discernible under these conditions, similar to the behavior of the $Al_{0.05}(TiVNb)_{0.90}Mo_{0.05}$ composition. These experiments clearly demonstrate that Mo addition results in a decrease in the temperature required to desorb hydrogen. Moreover, these results are in good agreement with both experimental and predicted thermodynamic values by data-driven models. Increasing Mo up to 10 at.% destabilizes the hydride so that desorption in the $Al_{0.05}(TiVNb)_{0.85}Mo_{0.10}$ composition occurs at lower temperatures. A similar decrease in the temperature of H_2 desorption was previously reported for $T_{0.325}V_{0.275}Zr_{0.125}Nb_{0.275}$ [29] and $Ti_{0.20}Zr_{0.20}Hf_{0.20}Nb_{0.40}$ phases [26] with increasing Mo content.

4. CONCLUSIONS

In the search for destabilized but high-capacity hydrides based on HEAs, we investigated the effect of Mo addition on the phase, microstructure, and hydrogen storage properties of $Al_{0.05}(TiVNb)_{0.95}$. The $Al_{0.05}(TiVNb)_{0.95-x}Mo_x$ (x=0.05, 0.10) alloys crystallize in a *bcc* lattice with a decreasing lattice parameter with increasing Mo content and a dendritic microstructure typical of refractory HEAs synthetized by arc melting. Dihydride formation occurs via a two-step reaction observed in the PCI experiments, which is typical for *bcc* alloys and the $Al_{0.05}(TiVNb)_{0.95}$ alloy. The maximum capacity gravimetric slightly decreases by Mo addition due to its heavy nature Equilibrium plateau pressures increase with the addition of Mo (*i.e.*, thermodynamic destabilization of the hydride), a trend which is qualitatively and quantitatively consistent with data-driven models for metal hydride thermodynamics. A hydride formation enthalpy (ΔH_{abs}) of -37±1 kJ/mol H_2 and a hydride desorption enthalpy (ΔH_{des}) of 47(±1.3) kJ/mol H_2 were obtained in $Al_{0.05}(TiVNb)_{0.85}Mo_{0.10}$. *Ex situ* neutron diffraction reveals deuterium localization at the tetrahedral sites of the *fcc* phase via deuterium absorption. The shift to lower desorption temperatures with increasing Mo content was further demonstrated by *in situ* Synchrotron-X-ray diffraction/neutron diffraction and thermo-desorption spectroscopy experiments. After desorption, the *bcc* phase is completely recovered with lattice parameters similar to the as-cast materials. Therefore, the simultaneous addition of non-forming hydrides such as Al and Mo to refractory HEAs in limited amounts can greatly improve the hydride thermodynamics without capacity loss.

These findings provide an important addition to the toolkit of strategies available for the design of high-entropy hydrides targeted for specific hydrogen use cases.

Supporting Information

Figure SI1. XRD patterns (λ = 1.5406 Å) and corresponding Rietveld refinement analysis for pristine alloys (a) $Al_{0.05}(TiVNb)_{0.90}Mo_{0.05}$ and (b) $Al_{0.05}(TiVNb)_{0.85}Mo_{0.10}$. **Figure SI2**. XRD patterns (λ= 1.5406 Å) and corresponding Rietveld refinement analysis for hydrides (a) $Al_{0.05}(TiVNb)_{0.90}Mo_{0.05}H_{1.78}$ and (b) $Al_{0.05}(TiVNb)_{0.85}Mo_{0.10}H_{1.79}$. **Figure SI3**. *Ex situ* powder nD pattern (λ=1.28 Å) of fully deuterated $Al_{0.05}(TiVNb)_{0.95}D_{1.81}$, corresponding Rietveld refinement analysis and lattice parameter. **Figure SI4.** PCIs of desorption at different temperatures of (a) $Al_{0.05}(TiVNb)_{0.90}Mo_{0.05}$ and (b) $Al_{0.05}(TiVNb)_{0.85}Mo_{0.10}$ with a range from 75 °C to 125 °C and 50 °C to 80 °C, respectively. (c) Van't Hoff plots for $Al_{0.05}(TiVNb)_{0.95-x}Mo_x$ (x=0.05,0.10). **Figure SI5.** *In situ* nD thermo-diffractogram (λ= 1.28 Å) of fully deuterated sample $Al_{0.05}(TiVNb)_{0.95}D_{1.81}$. **Figure SI6**. TDS profiles for (a) $Al_{0.05}(TiVNb)_{0.90}Mo_{0.05}$ hydride and (b) $Al_{0.05}(TiVNb)_{0.85}Mo_{0.10}$ hydride, heating ramp 5 °C/min. **Figure SI7**. XRD patterns (λ = 1.5406 Å) and corresponding Rietveld refinement analysis for (a) $Al_{0.05}(TiVNb)_{0.90}Mo_{0.05}$ and (b) $Al_{0.05}(TiVNb)_{0.85}Mo_{0.10}$ after TDS desorption. **Figure SI8**. *In situ* SR-XRD pattern during desorption (λ= 0.67156 Å) and the corresponding Rietveld refinement analysis for the (a) $Al_{0.05}(TiVNb)_{0.90}Mo_{0.05}$ hydride, (b) desorbed $Al_{0.05}(TiVNb)_{0.90}Mo_{0.05}$, (c) $Al_{0.05}(TiVNb)_{0.85}Mo_{0.10}$ hydride and (d) desorbed $Al_{0.05}(TiVNb)_{0.85}Mo_{0.10}$, everything at 25 °C. **Table SI1**. Lattice parameters of the $Al_{0.05}(TiVNb)_{0.95-x}Mo_x$ (x=0.05,0.10) alloys from in situ SR-XRD.

AUTHOR INFORMATION

Corresponding Author

* Corresponding author: claudia.zlotea@cnrs.fr.

Author Contributions

Conceptualization: C.Z. and N.P.-R.; formal analysis: N.P.-R. and C.Z.; investigation & methodology: N.P.-R., M.W., K.H., V.S., V.N., E.E. and C.Z.; supervision, validation: C.Z.; writing—original draft: N.P.-R., M.W., K.H., V.S. and C.Z.; writing—review & editing: N.P.-R., M.W., K.H., V.S., V.N., E.E. and C.Z. All authors have read and agreed to the published version of the manuscript.

Funding Sources

This research was funded by ANR MASSHY project ANR-19-CE05-0029-01.

ACKNOWLEDGMENT

We acknowledge the SOLEIL Synchrotron for the time allocation on the CRISTAL beamline. In the framework of the CNRS ßÉCIPROCS network, this work has been accepted for synchrotron beamtime by the Soleil scientific proposal committee (BAG proposal 20201440). The authors would like to thank Benoit Baptiste for the organization of the BAG (Block Allocation Group) beamtime at SOLEIL. Fabrice Couturas, Anis Bouzidi and Renato Belli Strozi from ICMPE are acknowledged for their help with the SR-XRD experiments and data treatment. We acknowledge the 2FDN for beamtime allocation on the CRG-D1B beamline. Inés Puente Orench from CSIC, Sofien Djellit from D1B, and Faye Greaves from ICMPE are acknowledged for their help with neutron diffraction experiments at ILL. We would like to thank Valérie Lalanne and Loïc Perrière from ICMPE, as well as Gustav Ek and Martin Sahlberg from Uppsala University, for their help with the arc melting. We also thank Rémy Pires for his help with SEM-EDX. Matthew Witman and Vitalie Stavila gratefully acknowledge research support from the U.S. Department of Energy, Office of Energy Efficiency and Renewable Energy, Hydrogen and Fuel Cell Technologies Office through the Hydrogen Storage Materials Advanced Research Consortium (HyMARC) and the Laboratory Directed Research and Development (LDRD) program at Sandia National Laboratories. Sandia National Laboratories is a multimission laboratory managed and operated by National Technology & Engineering Solutions of Sandia, LLC, a wholly owned subsidiary of Honeywell International Inc., for the U.S. Department of Energy's National Nuclear Security Administration (DOE/NNSA) under contract DE-NA0003525. This written work is authored by an employee of NTESS. The employee, not NTESS, owns the right, title and interest in and to the written work and is responsible for its contents. Any subjective views or opinions that might be expressed in the written work do not necessarily represent the views of the U.S. Government. The publisher acknowledges that the U.S. Government retains a non-exclusive, paid-up, irrevocable, world-wide license to publish or reproduce the published form of this written work or allow others to do so, for U.S. Government purposes. The DOE will provide public access to results of federally sponsored research in accordance with the DOE Public Access Plan.

REFERENCES

(1) Groll, M. Can Climate Change Be Avoided? Vision of a Hydrogen-Electricity Energy Economy. *Energy* **2023**, *264*, 126029. https://doi.org/10.1016/j.energy.2022.126029.

(2) Oliveira, A. M.; Beswick, R. R.; Yan, Y. A Green Hydrogen Economy for a Renewable Energy Society. *Current Opinion in Chemical Engineering* **2021**, *33*, 100701. https://doi.org/10.1016/j.coche.2021.100701.

(3) Woods, P.; Bustamante, H.; Aguey-Zinsou, K.-F. The Hydrogen Economy - Where Is the Water? *Energy Nexus* **2022**, *7*, 100123. https://doi.org/10.1016/j.nexus.2022.100123.

(4) Amirthan, T.; Perera, M. S. A. The Role of Storage Systems in Hydrogen Economy: A Review. *Journal of Natural Gas Science and Engineering* **2022**, *108*, 104843. https://doi.org/10.1016/j.jngse.2022.104843.

(5) Eberle, U.; Felderhoff, M.; Schüth, F. Chemical and Physical Solutions for Hydrogen Storage. *Angew. Chem. Int. Ed.* **2009**, *48* (36), 6608–6630. https://doi.org/10.1002/anie.200806293.

(6) Allendorf, M. D.; Stavila, V.; Snider, J. L.; Witman, M.; Bowden, M. E.; Brooks, K.; Tran, B. L.; Autrey, T. Challenges to Developing Materials for the Transport and Storage of Hydrogen. *Nat. Chem.* **2022**, *14* (11), 1214–1223. https://doi.org/10.1038/s41557-022-01056-2.

(7) Wang, Q.; Guo, J.; Chen, P. The Power of Hydrides. *Joule* **2020**, *4* (4), 705–709. https://doi.org/10.1016/j.joule.2020.02.008.

(8) Keith, A.; Zlotea, C.; Szilágyi, P. Á. Perspective of Interstitial Hydrides of High-Entropy Alloys for Vehicular Hydrogen Storage. *International Journal of Hydrogen Energy* **2023**, S0360319923002598. https://doi.org/10.1016/j.ijhydene.2023.01.141.

(9) Sahlberg, M.; Karlsson, D.; Zlotea, C.; Jansson, U. Superior Hydrogen Storage in High Entropy Alloys. *Sci Rep* **2016**, *6* (1), 36770. https://doi.org/10.1038/srep36770.

(10) Yeh, J.-W.; Chen, S.-K.; Lin, S.-J.; Gan, J.-Y.; Chin, T.-S.; Shun, T.-T.; Tsau, C.-H.; Chang, S.-Y. Nanostructured High-Entropy Alloys with Multiple Principal Elements: Novel Alloy Design Concepts and Outcomes. *Adv. Eng. Mater.* **2004**, *6* (5), 299–303. https://doi.org/10.1002/adem.200300567.

(11) Yang, X.; Zhang, Y. Prediction of High-Entropy Stabilized Solid-Solution in Multi-Component Alloys. *Materials Chemistry and Physics* **2012**, *132* (2–3), 233–238. https://doi.org/10.1016/j.matchemphys.2011.11.021.

(12) Zhang, Y.; Zhou, Y. J.; Lin, J. P.; Chen, G. L.; Liaw, P. K. Solid-Solution Phase Formation Rules for Multi-Component Alloys. *Adv. Eng. Mater.* **2008**, *10* (6), 534–538. https://doi.org/10.1002/adem.200700240.

(13) Guo, S.; Ng, C.; Lu, J.; Liu, C. T. Effect of Valence Electron Concentration on Stability of Fcc or Bcc Phase in High Entropy Alloys. *Journal of Applied Physics* **2011**, *109* (10), 103505. https://doi.org/10.1063/1.3587228.

(14) Kong, L.; Cheng, B.; Wan, D.; Xue, Y. A Review on BCC-Structured High-Entropy Alloys for Hydrogen Storage. *Front. Mater.* **2023**, *10*, 1135864. https://doi.org/10.3389/fmats.2023.1135864.

(15) El-Hadad, S. High Entropy Alloys: The Materials of Future. *International Journal of Materials Technology and Innovation* **2022**, *2* (1), 67–84. https://doi.org/10.21608/ijmti.2022.118565.1046.

(16) Witman, M. D.; Ling, S.; Wadge, M.; Bouzidi, A.; Pineda-Romero, N.; Clulow, R.; Ek, G.; Chames, J. M.; Allendorf, E. J.; Agarwal, S.; Allendorf, M. D.; Walker, G. S.; Grant, D. M.; Sahlberg, M.; Zlotea, C.; Stavila, V. Towards Pareto Optimal High Entropy Hydrides *via* Data-

Driven Materials Discovery. *J. Mater. Chem. A* **2023**, *11* (29), 15878–15888. https://doi.org/10.1039/D3TA02323K.

(17) Ek, G.; Nygård, M. M.; Pavan, A. F.; Montero, J.; Henry, P. F.; Sørby, M. H.; Witman, M.; Stavila, V.; Zlotea, C.; Hauback, B. C.; Sahlberg, M. Elucidating the Effects of the Composition on Hydrogen Sorption in TiVZrNbHf-Based High-Entropy Alloys. *Inorg. Chem.* **2021**, *60* (2), 1124–1132. https://doi.org/10.1021/acs.inorgchem.0c03270.

(18) Zlotea, C.; Sow, M. A.; Ek, G.; Couzinié, J.-P.; Perrière, L.; Guillot, I.; Bourgon, J.; Møller, K. T.; Jensen, T. R.; Akiba, E.; Sahlberg, M. Hydrogen Sorption in TiZrNbHfTa High Entropy Alloy. *Journal of Alloys and Compounds* **2019**, *775*, 667–674. https://doi.org/10.1016/j.jallcom.2018.10.108.

(19) Cheng, B.; Li, Y.; Li, X.; Ke, H.; Wang, L.; Cao, T.; Wan, D.; Wang, B.; Xue, Y. Solid-State Hydrogen Storage Properties of Ti–V–Nb–Cr High-Entropy Alloys and the Associated Effects of Transitional Metals (M = Mn, Fe, Ni). *Acta Metall. Sin. (Engl. Lett.)* **2022**. https://doi.org/10.1007/s40195-022-01403-9.

(20) Yang, F.; Wang, J.; Zhang, Y.; Wu, Z.; Zhang, Z.; Zhao, F.; Huot, J.; Grobivć Novaković, J.; Novaković, N. Recent Progress on the Development of High Entropy Alloys (HEAs) for Solid Hydrogen Storage: A Review. *International Journal of Hydrogen Energy* **2022**, *47* (21), 11236–11249. https://doi.org/10.1016/j.ijhydene.2022.01.141.

(21) Ferraz, M. de B.; Botta, W. J.; Zepon, G. Synthesis, Characterization and First Hydrogen Absorption/Desorption of the Mg35Al15Ti25V10Zn15 High Entropy Alloy. *International Journal of Hydrogen Energy* **2022**, *47* (54), 22881–22892. https://doi.org/10.1016/j.ijhydene.2022.05.098.

(22) Montero, J.; Ek, G.; Sahlberg, M.; Zlotea, C. Improving the Hydrogen Cycling Properties by Mg Addition in Ti-V-Zr-Nb Refractory High Entropy Alloy. *Scripta Materialia* **2021**, *194*, 113699. https://doi.org/10.1016/j.scriptamat.2020.113699.

(23) Montero, J.; Ek, G.; Laversenne, L.; Nassif, V.; Sahlberg, M.; Zlotea, C. How 10 At% Al Addition in the Ti-V-Zr-Nb High-Entropy Alloy Changes Hydrogen Sorption Properties. *Molecules* **2021**, *26* (9), 2470. https://doi.org/10.3390/molecules26092470.

(24) Pineda-Romero, N.; Zlotea, C. Uncovering the Effect of Al Addition on the Hydrogen Storage Properties of the Ternary TiVNb Alloy. *Materials* **2022**, *15* (22), 7974. https://doi.org/10.3390/ma15227974.

(25) Sabeena, M.; Murugesan, S.; Anees, P.; Mohandas, E.; Vijayalakshmi, M. Crystal Structure and Bonding Characteristics of Transformation Products of Bcc β in Ti-Mo Alloys. *Journal of Alloys and Compounds* **2017**, *705*, 769–781. https://doi.org/10.1016/j.jallcom.2016.12.155.

(26) Shen, H.; Hu, J.; Li, P.; Huang, G.; Zhang, J.; Zhang, J.; Mao, Y.; Xiao, H.; Zhou, X.; Zu, X.; Long, X.; Peng, S. Compositional Dependence of Hydrogenation Performance of Ti-Zr-Hf-Mo-Nb High-Entropy Alloys for Hydrogen/Tritium Storage. *Journal of Materials Science & Technology* **2020**, *55*, 116–125. https://doi.org/10.1016/j.jmst.2019.08.060.

(27) Ferreira, T.; Pineda-Romero, N.; Botta, W. J.; Zepon, G.; Zlotea, C. Tuning the Hydride Stability of the TiVNb-Based Alloys by Equimolar Cr/Al Addition. *Intermetallics* **2023**, *161*, 107992. https://doi.org/10.1016/j.intermet.2023.107992.

(28) Montero, J.; Zlotea, C.; Ek, G.; Crivello, J.-C.; Laversenne, L.; Sahlberg, M. TiVZrNb Multi-Principal-Element Alloy: Synthesis Optimization, Structural, and Hydrogen Sorption Properties. *Molecules* **2019**, *24* (15), 2799. https://doi.org/10.3390/molecules24152799.

(29) Bouzidi, A.; Laversenne, L.; Zepon, G.; Vaughan, G.; Nassif, V.; Zlotea, C. Hydrogen Sorption Properties of a Novel Refractory Ti-V-Zr-Nb-Mo High Entropy Alloy. *Hydrogen* **2021**, *2* (4), 399–413. https://doi.org/10.3390/hydrogen2040022.

(30) Royal Society of Chemistry. *Periodic Table*. https://www.rsc.org/periodic-table/.

(31) Zlotea, C.; Couturas, F.; Greaves, F.; Nassif, V.; Pineda-Romero, N. In Situ Hydrogen Desorption Study from High Entropy Hydrides: Effect of Addition of Non-Absorbing Elements (Al, Cr, Mo) in the TiVNb Alloy. https://doi.org/10.5291/ILL-DATA.5-25-284.

(32) Zlotea, C.; Oumellal, Y.; Msakni, M.; Bourgon, J.; Bastide, S.; Cachet-Vivier, C.; Latroche, M. First Evidence of Rh Nano-Hydride Formation at Low Pressure. *Nano Lett.* **2015**, *15* (7), 4752–4757. https://doi.org/10.1021/acs.nanolett.5b01766.

(33) Chen, S. Y.; Yang, X.; Dahmen, K. A.; Liaw, P. K.; Zhang, Y. Microstructures and Crackling Noise of AlxNbTiMoV High Entropy Alloys. *Entropy* **2014**, *16* (2), 870–884. https://doi.org/10.3390/e16020870.

(34) Chen, L.; Wang, Y.; Hao, X.; Zhang, X.; Liu, H. Lightweight Refractory High Entropy Alloy Coating by Laser Cladding on Ti–6Al–4V Surface. *Vacuum* **2021**, *183*, 109823. https://doi.org/10.1016/j.vacuum.2020.109823.

(35) Xu, Z. Q.; Ma, Z. L.; Wang, M.; Chen, Y. W.; Tan, Y. D.; Cheng, X. W. Design of Novel Low-Density Refractory High Entropy Alloys for High-Temperature Applications. *Materials Science and Engineering: A* **2019**, *755*, 318–322. https://doi.org/10.1016/j.msea.2019.03.054.

(36) Miracle, D. B.; Senkov, O. N. A Critical Review of High Entropy Alloys and Related Concepts. *Acta Materialia* **2017**, *122*, 448–511. https://doi.org/10.1016/j.actamat.2016.08.081.

(37) Hu, H.; Ma, C.; Zhou, L.; Xiao, H.; Chen, Q. Understanding Crystal Structure Roles towards Developing High-Performance V-Free BCC Hydrogen Storage Alloys. *International Journal of Hydrogen Energy* **2022**, *47* (60), 25335–25346. https://doi.org/10.1016/j.ijhydene.2022.05.241.

(38) Couzinié, J.-P.; Senkov, O. N.; Miracle, D. B.; Dirras, G. Comprehensive Data Compilation on the Mechanical Properties of Refractory High-Entropy Alloys. *Data in Brief* **2018**, *21*, 1622–1641. https://doi.org/10.1016/j.dib.2018.10.071.

(39) Couzinié, J. P.; Dirras, G.; Perrière, L.; Chauveau, T.; Leroy, E.; Champion, Y.; Guillot, I. Microstructure of a Near-Equimolar Refractory High-Entropy Alloy. *Materials Letters* **2014**, *126*, 285–287. https://doi.org/10.1016/j.matlet.2014.04.062.

(40) Laurent-Brocq, M.; Akhatova, A.; Perrière, L.; Chebini, S.; Sauvage, X.; Leroy, E.; Champion, Y. Insights into the Phase Diagram of the CrMnFeCoNi High Entropy Alloy. *Acta Materialia* **2015**, *88*, 355–365. https://doi.org/10.1016/j.actamat.2015.01.068.

(41) Gross, K. J.; Russell Carrington, K.; Barcelo, S.; Karkamkar, A.; Purewal, J.; Ma, S.; Zhou, H.-C.; Dantzer, P.; Ott, K.; Burrell, T.; Semeslberger, T.; Pivak, Y.; Dam, B.; Chandra, D. *Recommended Best Practices for the Characterization of Storage Properties of Hydrogen Storage Materials*. U.S. Department of Energy Office of Energy Efficiency & Renewable Energy. https://www.energy.gov/eere/fuelcells/articles/recommended-best-practices-characterization-storage-properties-hydrogen-0.

(42) Kunce, I.; Polanski, M.; Bystrzycki, J. Microstructure and Hydrogen Storage Properties of a TiZrNbMoV High Entropy Alloy Synthesized Using Laser Engineered Net Shaping (LENS). *International Journal of Hydrogen Energy* **2014**, *39* (18), 9904–9910. https://doi.org/10.1016/j.ijhydene.2014.02.067.

(43) Sleiman, S.; Huot, J. Microstructure and First Hydrogenation Properties of TiHfZrNb1−xV1+x Alloy for x = 0, 0.1, 0.2, 0.4, 0.6 and 1. *Molecules* **2022**, *27* (3), 1054. https://doi.org/10.3390/molecules27031054.

(44) Montero, J.; Ek, G.; Laversenne, L.; Nassif, V.; Zepon, G.; Sahlberg, M.; Zlotea, C. Hydrogen Storage Properties of the Refractory Ti–V–Zr–Nb–Ta Multi-Principal Element Alloy. *Journal of Alloys and Compounds* **2020**, *835*, 155376. https://doi.org/10.1016/j.jallcom.2020.155376.

(45) Shen, H.; Zhang, J.; Hu, J.; Zhang, J.; Mao, Y.; Xiao, H.; Zhou, X.; Zu, X. A Novel TiZrHfMoNb High-Entropy Alloy for Solar Thermal Energy Storage. *Nanomaterials* **2019**, *9* (2), 248. https://doi.org/10.3390/nano9020248.

(46) *Neutron Applications in Earth, Energy and Environmental Sciences*; Liang, L., Rinaldi, R., Schober, H., Eds.; Neutron Scattering Applications and Techniques; Springer: New York, NY, 2009.

(47) Hattrick-Simpers, J. R.; Choudhary, K.; Corgnale, C. A Simple Constrained Machine Learning Model for Predicting High-Pressure-Hydrogen-Compressor Materials. *Mol. Syst. Des. Eng.* **2018**, *3* (3), 509–517. https://doi.org/10.1039/C8ME00005K.

(48) Witman, M.; Ling, S.; Grant, D. M.; Walker, G. S.; Agarwal, S.; Stavila, V.; Allendorf, M. D. Extracting an Empirical Intermetallic Hydride Design Principle from Limited Data via Interpretable Machine Learning. *J. Phys. Chem. Lett.* **2020**, *11* (1), 40–47. https://doi.org/10.1021/acs.jpclett.9b02971.

(49) Witman, M.; Ek, G.; Ling, S.; Chames, J.; Agarwal, S.; Wong, J.; Allendorf, M. D.; Sahlberg, M.; Stavila, V. Data-Driven Discovery and Synthesis of High Entropy Alloy Hydrides with Targeted Thermodynamic Stability. *Chem. Mater.* **2021**, *33* (11), 4067–4076. https://doi.org/10.1021/acs.chemmater.1c00647.

(50) Witman, M.; Allendorf, M.; Stavila, V. Database for Machine Learning of Hydrogen Storage Materials Properties, 2022. https://doi.org/10.5281/ZENODO.7293044.

(51) Yartys, V. A.; Lototskyy, M. V. Laves Type Intermetallic Compounds as Hydrogen Storage Materials: A Review. *Journal of Alloys and Compounds* **2022**, *916*, 165219. https://doi.org/10.1016/j.jallcom.2022.165219.

(52) Nakamura, Y.; Oikawa, K.; Kamiyama, T.; Akiba, E. Crystal Structure of Two Hydrides Formed from a Ti–V–Mn BCC Solid Solution Alloy Studied by Time-of-Flight Neutron Powder Diffraction — a NaCl Structure and a CaF2 Structure. *Journal of Alloys and Compounds* **2001**, *316* (1–2), 284–289. https://doi.org/10.1016/S0925-8388(00)01503-6.

(53) Callear, S. K.; Ramirez-Cuesta, A. J.; Kamazawa, K.; Towata, S.; Noritake, T.; Parker, S. F.; Jones, M. O.; Sugiyama, J.; Ishikiriyama, M.; David, W. I. F. Understanding Composition–Property Relationships in Ti–Cr–V–Mo Alloys for Optimisation of Hydrogen Storage in Pressurised Tanks. *Phys. Chem. Chem. Phys.* **2014**, *16* (31), 16563–16572. https://doi.org/10.1039/C4CP01666A.

(54) Akiba, E.; Okada, M. Metallic Hydrides III: Body-Centered-Cubic Solid-Solution Alloys. *MRS Bull.* **2002**, *27* (9), 699–703. https://doi.org/10.1557/mrs2002.225.

(55) Bouzidi, A.; Laversenne, L.; Nassif, V.; Elkaim, E.; Zlotea, C. Hydrogen Storage Properties of a New Ti-V-Cr-Zr-Nb High Entropy Alloy. *Hydrogen* **2022**, *3* (2), 270–284. https://doi.org/10.3390/hydrogen3020016.

(56) Pineda-Romero, N.; Witman, M.; Stavila, V.; Zlotea, C. The Effect of 10 at.% Al Addition on the Hydrogen Storage Properties of the Ti0.33V0.33Nb0.33 Multi-Principal Element Alloy. *Intermetallics* **2022**, *146*, 107590. https://doi.org/10.1016/j.intermet.2022.107590.

(57) Strozi, R. B.; Leiva, D. R.; Zepon, G.; Botta, W. J.; Huot, J. Effects of the Chromium Content in (TiVNb)100−xCrx Body-Centered Cubic High Entropy Alloys Designed for Hydrogen Storage Applications. *Energies* **2021**, *14* (11), 3068. https://doi.org/10.3390/en14113068.

(58) Nygård, M. M.; Fjellvåg, Ø. S.; Sørby, M. H.; Sakaki, K.; Ikeda, K.; Armstrong, J.; Vajeeston, P.; Sławiński, W. A.; Kim, H.; Machida, A.; Nakamura, Y.; Hauback, B. C. The Average and Local Structure of TiVCrNbD x (x = 0 , 2.2 , 8) from Total Scattering and Neutron Spectroscopy. *Acta Materialia* **2021**, *205*, 116496. https://doi.org/10.1016/j.actamat.2020.116496.

(59) Strozi, R. B.; Silva, B. H.; Leiva, D. R.; Zlotea, C.; Botta, W. J.; Zepon, G. Tuning the Hydrogen Storage Properties of Ti-V-Nb-Cr Alloys by Controlling the Cr/(TiVNb) Ratio. *Journal of Alloys and Compounds* **2023**, *932*, 167609. https://doi.org/10.1016/j.jallcom.2022.167609.

(60) Akiba, E. *Energy Carriers and Conversion Systems-Physics of Metal Hydrides*; Ohta, T., Ed.; Encyclopedia of life support systems ; Energy sciences, engineering, and technology resources; Eolss Publishers: Oxford, U.K, 2009; Vol. II.

(61) Senkov, O. N.; Senkova, S. V.; Woodward, C. Effect of Aluminum on the Microstructure and Properties of Two Refractory High-Entropy Alloys. *Acta Materialia* **2014**, *68*, 214–228. https://doi.org/10.1016/j.actamat.2014.01.029.

(62) He, J. Y.; Liu, W. H.; Wang, H.; Wu, Y.; Liu, X. J.; Nieh, T. G.; Lu, Z. P. Effects of Al Addition on Structural Evolution and Tensile Properties of the FeCoNiCrMn High-Entropy Alloy System. *Acta Materialia* **2014**, *62*, 105–113. https://doi.org/10.1016/j.actamat.2013.09.037.

(63) Murty, B. S.; Yeh, J. W.; Ranganathan, S. High-Entropy Alloy Solid Solutions. In *High Entropy Alloys*; Elsevier, 2014; pp 91–118. https://doi.org/10.1016/B978-0-12-800251-3.00006-7.

(64) Buschow, K. H. J.; Bouten, P. C. P.; Miedema, A. R. Hydrides Formed from Intermetallic Compounds of Two Transition Metals: A Special Class of Ternary Alloys. *Rep. Prog. Phys.* **1982**, *45* (9), 937–1039. https://doi.org/10.1088/0034-4885/45/9/001.

(65) Andreasen, A. *Predicting Formation Enthalpies of Metal Hydrides*; Risø National Laboratory: Denmark, 2004.

(66) Strozi, R. B.; Witman, M.; Stavila, V.; Cizek, J.; Sakaki, K.; Kim, H.; Melikhova, O.; Perrière, L.; Machida, A.; Nakahira, Y.; Zepon, G.; Botta, W. J.; Zlotea, C. Elucidating Primary Degradation Mechanisms in High-Cycling-Capacity, Compositionally Tunable High-Entropy Hydrides. *ACS Appl. Mater. Interfaces* **2023**, *15* (32), 38412–38422. https://doi.org/10.1021/acsami.3c05206.

(67) Silva, B. H.; Zlotea, C.; Champion, Y.; Botta, W. J.; Zepon, G. Design of TiVNb-(Cr, Ni or Co) Multicomponent Alloys with the Same Valence Electron Concentration for Hydrogen Storage. *Journal of Alloys and Compounds* **2021**, *865*, 158767. https://doi.org/10.1016/j.jallcom.2021.158767.

Table of content

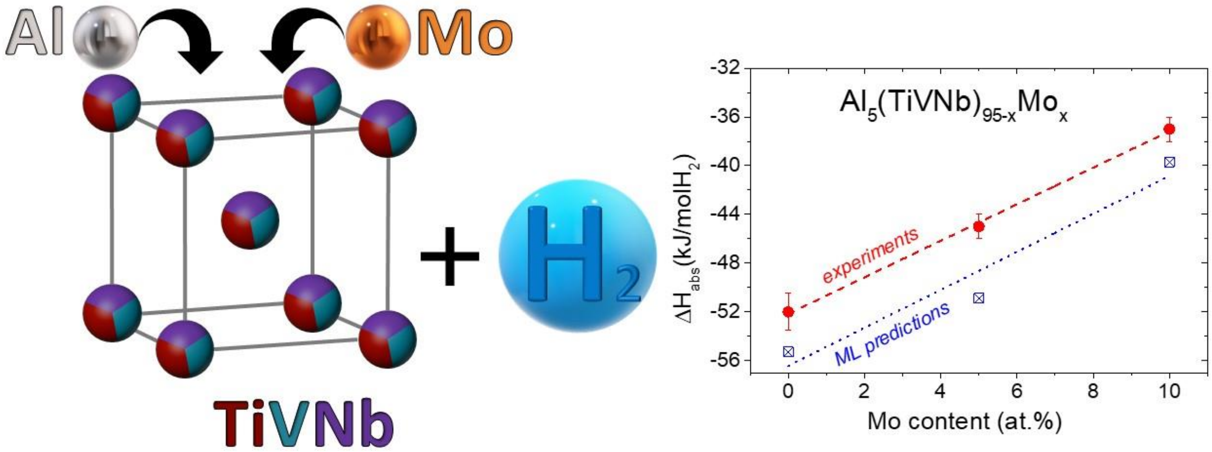

Both experiments and machine learning predictions agree to demonstrate strong thermodynamic destabilization of hydride formation by small additions of Mo and Al in TiVNb

Supplementary information

Large destabilization of (TiVNb)-based hydrides via (Al, Mo) addition: insights from experiments and data-driven models

*Nayely Pineda Romero[1], Matthew Witman[2], Kim Harvey[2], Vitalie Stavila[2], Vivian Nassif[3], Erik Elkaïm[4] and Claudia Zlotea[1]**

Corresponding author email: claudia.zlotea@cnrs.fr

[1]Univ Paris Est Creteil, CNRS, ICMPE, UMR 7182, 2 rue Henri Dunant, 94320 Thiais, France

[2]Sandia National Laboratories, Livermore, CA, 94551, United States.

[3]University Grenoble Alpes, CNRS, Grenoble INP, Institut Néel, 38000 Grenoble, France.

[4]Synchrotron SOLEIL, L'Orme des Merisiers, Saint-Aubin, BP48, 91192 Gif sur Yvette, France.

Figure SI1. XRD patterns (λ = 1.5406 Å) and corresponding Rietveld refinement analysis for pristine alloys (a) $Al_{0.05}(TiVNb)_{0.90}Mo_{0.05}$ and (b) $Al_{0.05}(TiVNb)_{0.85}Mo_{0.10}$.

Figure SI2. XRD patterns (λ = 1.5406 Å) and corresponding Rietveld refinement analysis for hydrides (a) $Al_{0.05}(TiVNb)_{0.90}Mo_{0.05}H_{1.78}$ and (b) $Al_{0.05}(TiVNb)_{0.85}Mo_{0.10}H_{1.79}$.

Figure SI3. Ex situ powder nD pattern (λ=1.28 Å) of fully deuterated $Al_{0.05}(TiVNb)_{0.95}D_{1.81}$, corresponding Rietveld refinement analysis and lattice parameter.

Figure SI4. PCIs of desorption at different temperatures of (a) $Al_{0.05}(TiVNb)_{0.90}Mo_{0.05}$ and (b) $Al_{0.05}(TiVNb)_{0.85}Mo_{0.10}$ with a range from 75 °C to 125 °C and 50 °C to 80 °C, respectively. (c) Van't Hoff plots for $Al_{0.05}(TiVNb)_{0.95-x}Mo_x$ (x=0.05,0.10).

Figure SI5. In situ nD thermo-diffractogram (λ= 1.28 Å) of fully deuterated sample $Al_{0.05}(TiVNb)_{0.95}D_{1.81}$.

Figure SI6. TDS profiles for (a) $Al_{0.05}(TiVNb)_{0.90}Mo_{0.05}$ hydride and (b) $Al_{0.05}(TiVNb)_{0.85}Mo_{0.10}$ hydride, heating ramp 5 °C/min.

Figure SI7. XRD patterns (λ = 1.5406 Å) and corresponding Rietveld refinement analysis for (a) $Al_{0.05}(TiVNb)_{0.90}Mo_{0.05}$ and (b) $Al_{0.05}(TiVNb)_{0.85}Mo_{0.10}$ after TDS desorption.

Figure SI8. In situ SR-XRD pattern during desorption (λ= 0.67156 Å) and the corresponding Rietveld refinement analysis for the (a) $Al_{0.05}(TiVNb)_{0.90}Mo_{0.05}$ hydride, (b) desorbed $Al_{0.05}(TiVNb)_{0.90}Mo_{0.05}$, (c) $Al_{0.05}(TiVNb)_{0.85}Mo_{0.10}$ hydride and (d) desorbed $Al_{0.05}(TiVNb)_{0.85}Mo_{0.10}$, everything at 25 °C.

Table SI1. Lattice parameters of the $Al_{0.05}(TiVNb)_{0.95-x}Mo_x$ (x=0.05,0.10) alloys from in situ SR-XRD.

Figure SI1. XRD patterns (λ = 1.5406 Å) and corresponding Rietveld refinement analysis for pristine alloys (a) $Al_{0.05}(TiVNb)_{0.90}Mo_{0.05}$ and (b) $Al_{0.05}(TiVNb)_{0.85}Mo_{0.10}$.

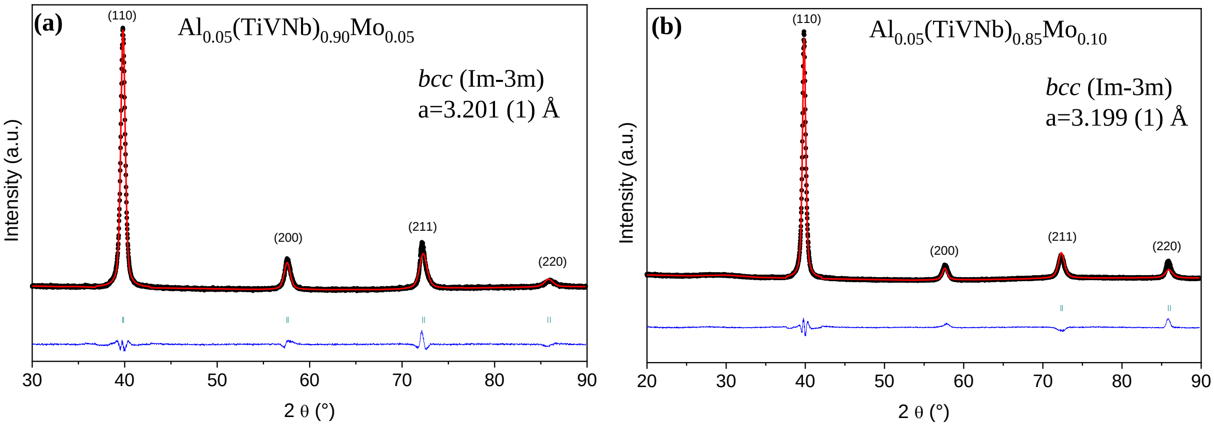

Figure SI2. XRD patterns (λ = 1.5406 Å) and corresponding Rietveld refinement analysis for hydrides (a) $Al_{0.05}(TiVNb)_{0.90}Mo_{0.05}H_{1.78}$ and (b) $Al_{0.05}(TiVNb)_{0.85}Mo_{0.10}H_{1.79}$.

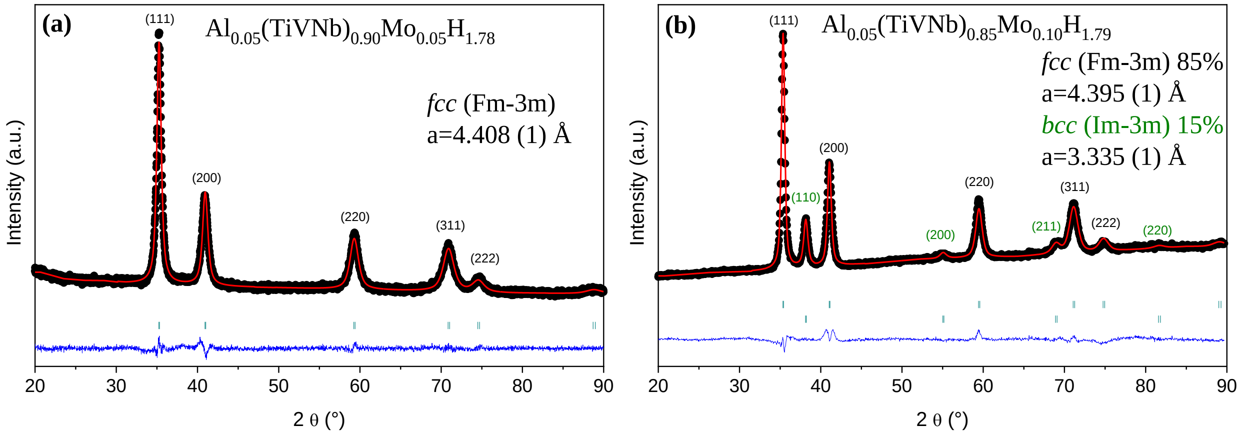

Figure SI3. Ex situ powder nD pattern (λ=1.28 Å) of fully deuterated $Al_{0.05}(TiVNb)_{0.95}D_{1.81}$, corresponding Rietveld refinement analysis and lattice parameter.

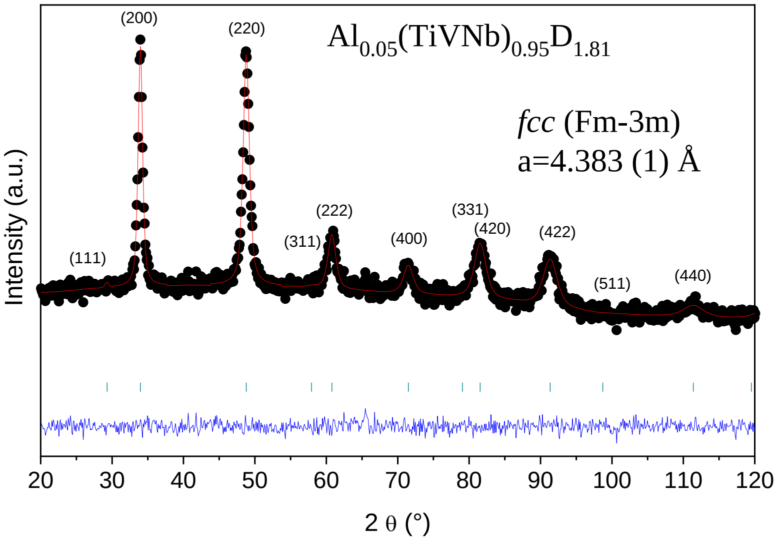

Figure SI4. PCIs of desorption at different temperatures of (a) $Al_{0.05}(TiVNb)_{0.90}Mo_{0.05}$ and (b) $Al_{0.05}(TiVNb)_{0.85}Mo_{0.10}$ with a range from 75 °C to 125 °C and 50 °C to 80 °C, respectively. (c) Van't Hoff plots for $Al_{0.05}(TiVNb)_{0.95-x}Mo_x$ (x=0.05,0.10).

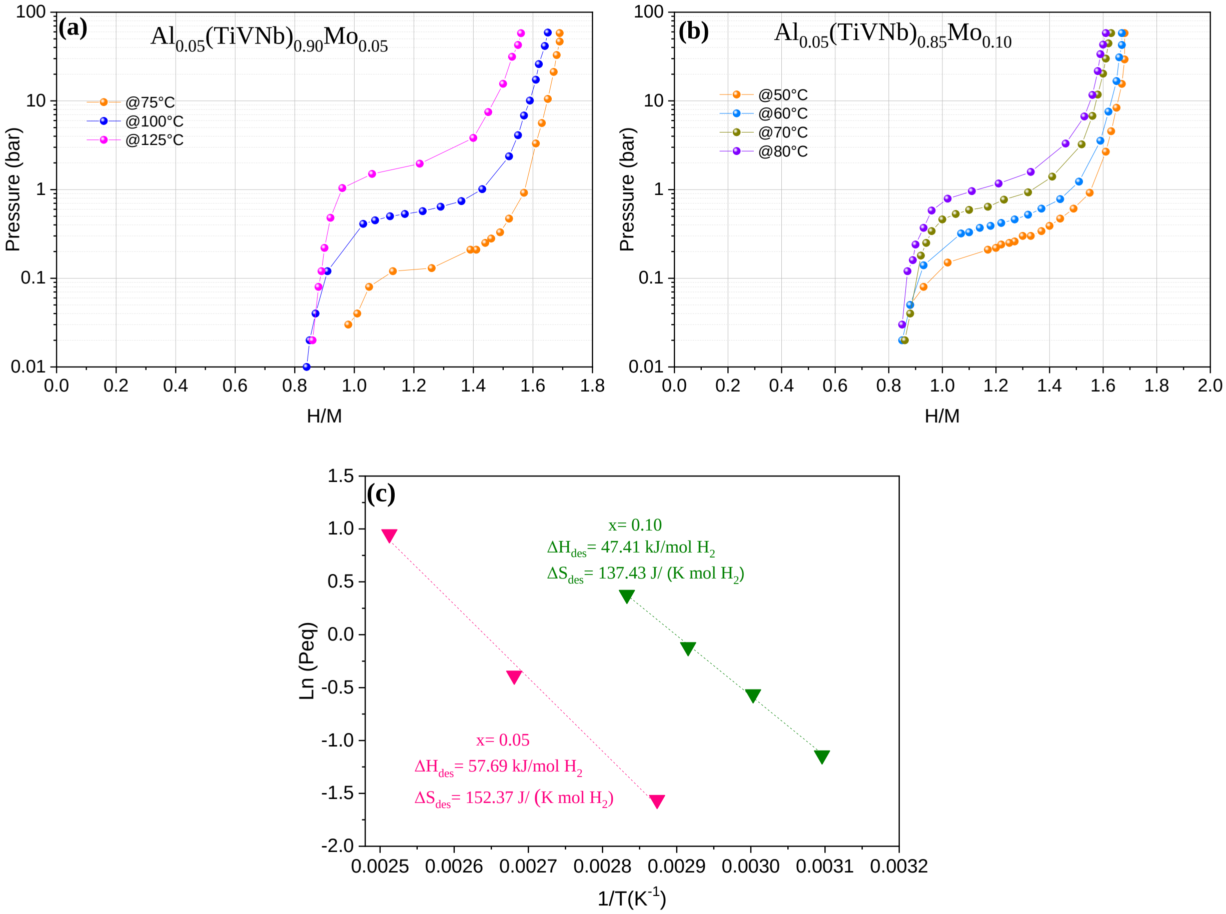

Figure SI5. In situ nD thermo-diffractogram (λ= 1.28 Å) of fully deuterated sample $Al_{0.05}(TiVNb)_{0.95}D_{1.81}$.

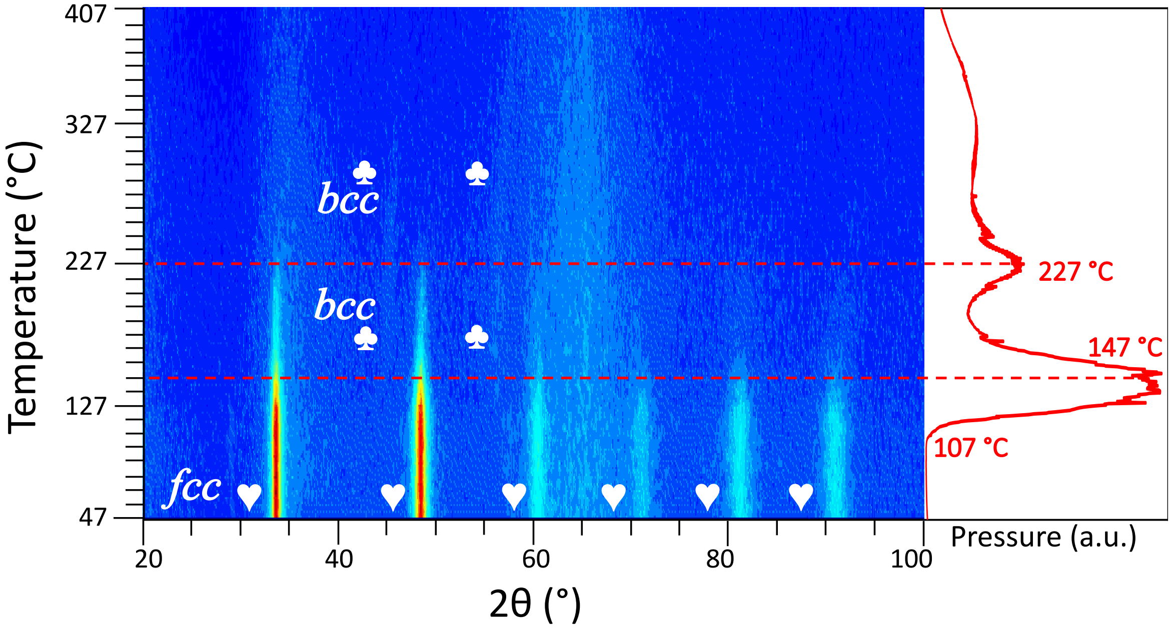

In situ neutron thermo-diffractogram of the $Al_{0.05}(TiVNb)_{0.95}D_{1.81}$ is shown in Figure SI5. The initial *fcc* phase (marked with ♥) is stable up to around 107 °C and it is shown a drastic decrease of the intensity peaks about 147 °C when the desorption profile shows the main peak. Above 147 °C is shown the formation of the *bcc* phase (marked with ♣). In the temperature range from 147 °C to 227 °C there is a coexistence of the *fcc* phase and the *bcc* desorbed phase. Then, at about 227 °C it is observed that the *fcc* phase disappears completely and the second peak in the pressure profile is observed. Above this temperature only the *bcc* phase is recovered with a shift towards higher 2θ (°).

Figure SI6. TDS profiles for (a) $Al_{0.05}(TiVNb)_{0.90}Mo_{0.05}$ hydride and (b) $Al_{0.05}(TiVNb)_{0.85}Mo_{0.10}$ hydride, heating ramp 5 °C/min.

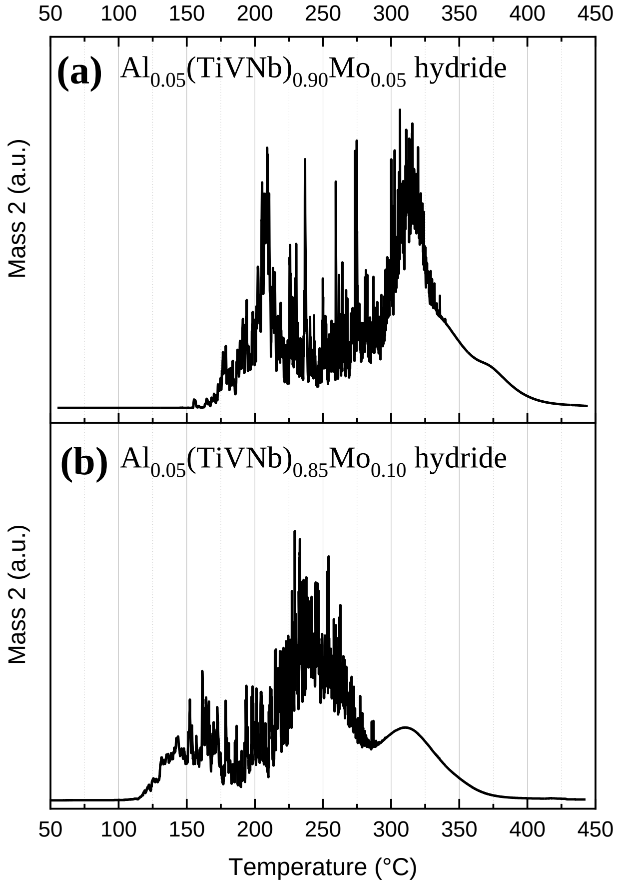

TDS was carried out with a heating ramp of 5 °C/min. The profile of $Al_{0.05}(TiVNb)_{0.90}Mo_{0.05}$ hydride (Figure SI6a) indicates a desorption onset temperature of around 174 °C with the first desorption event followed by a second one with a maximum temperature at 306 °C which ends around 400 °C. Besides, $Al_{0.05}(TiVNb)_{0.85}Mo_{0.10}$ hydride (Figure SI6b) indicates a desorption onset temperature of around 116 °C with a broad event continued by a second event with a maximum temperature about 229 °C and a small event at 310 °C which ends around 400 °C.

Figure SI7. XRD patterns (λ = 1.5406 Å) and corresponding Rietveld refinement analysis for (a) $Al_{0.05}(TiVNb)_{0.90}Mo_{0.05}$ and (b) $Al_{0.05}(TiVNb)_{0.85}Mo_{0.10}$ after TDS desorption.

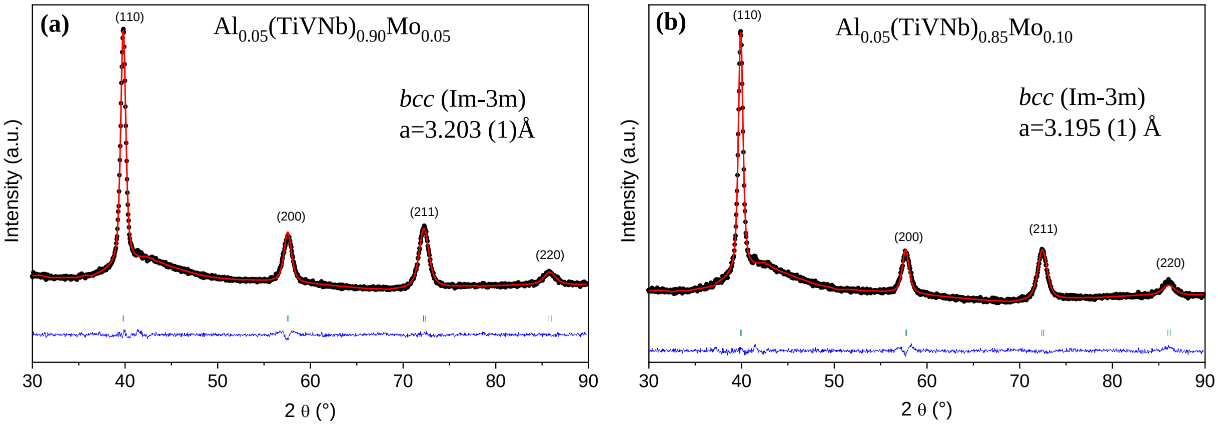

After TDS analysis, the XRD patterns (Figure SI7 a and b) show complete recovery of the initial *bcc* phase, but we can observe a broad peak just after the (110). This effect is due to the quartz wool used during the experiment to avoid powder loss with the vacuum environment. When XRD analysis is performed, there are few residues from the quartz wool that cannot be removed.

Figure SI8. In situ SR-XRD pattern during desorption (λ= 0.67156 Å) and the corresponding Rietveld refinement analysis for the (a) $Al_{0.05}(TiVNb)_{0.90}Mo_{0.05}$ hydride, (b) desorbed $Al_{0.05}(TiVNb)_{0.90}Mo_{0.05}$, (c) $Al_{0.05}(TiVNb)_{0.85}Mo_{0.10}$ hydride and (d) desorbed $Al_{0.05}(TiVNb)_{0.85}Mo_{0.10}$, everything at 25 °C.

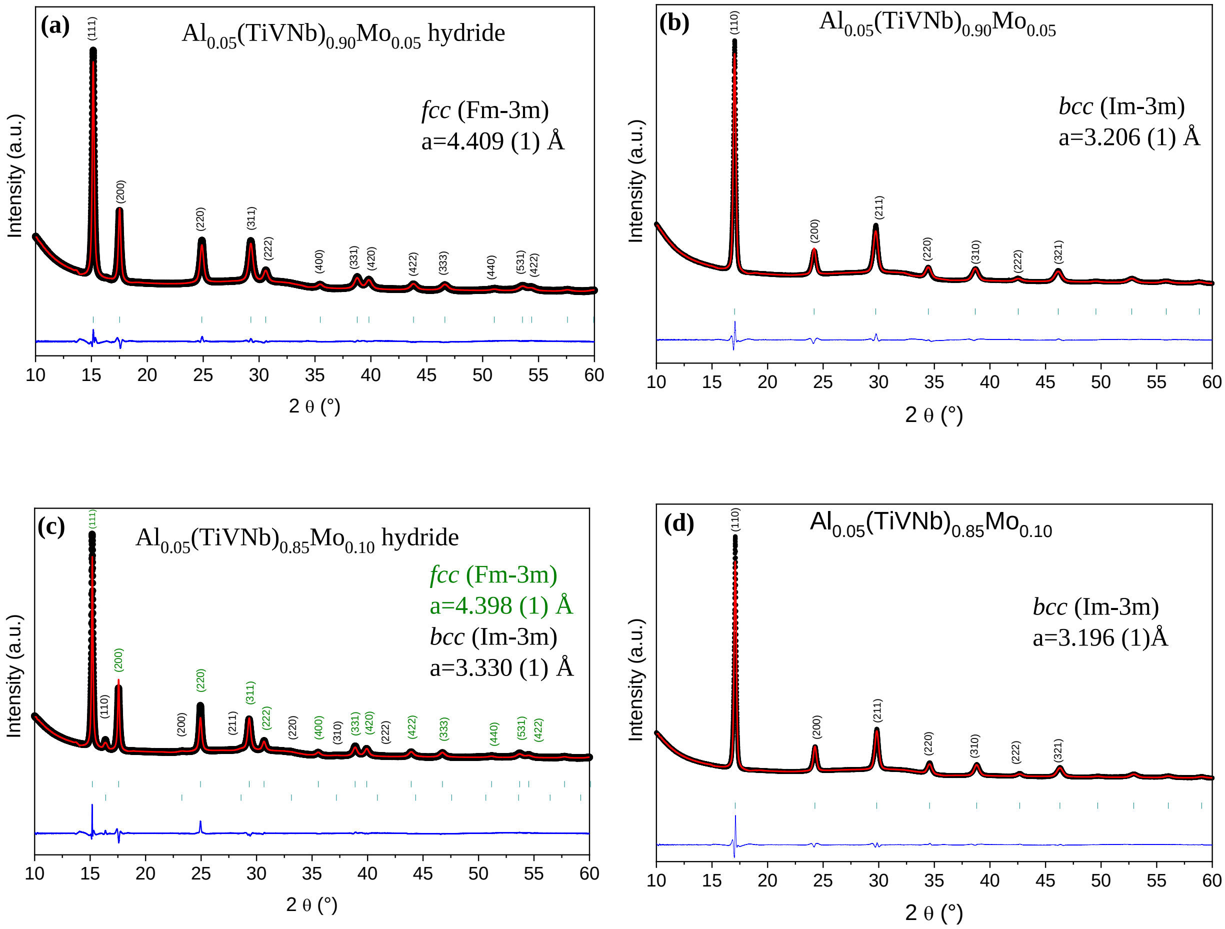

Table SI1. Lattice parameters of the $Al_{0.05}(TiVNb)_{0.95-x}Mo_x$ (x=0.05,0.10) alloys from in situ SR-XRD.

Composition	Form	Phase structure	Phase fraction (%)	Lattice parameter (Å)	Temperature (°C)
$Al_{0.05}(TiVNb)_{0.90}Mo_{0.05}$	dihydride	*fcc*	100	4.409(1)	25
		fcc	100	4.411(1)	151
		fcc	100	4.410(1)	200
	fcc + *bcc* mixture	*fcc*	98	4.407(1)	227
		bcc	2	3.348(1)	
		fcc	87.5	4.403(1)	254
		bcc	12.5	3.341(1)	
		fcc	51	4.396(1)	276
		bcc	49	3.328(1)	
		fcc	32	4.393(1)	285
		bcc	68	3.322(1)	
		fcc	8	4.388(1)	303
		bcc	92	3.305(1)	
		fcc	1	4.386(1)	320
		bcc	99	3.286(1)	
	desorbed *bcc*	*bcc*	100	3.277(1)	329
		bcc	100	3.262(1)	347
		bcc	100	3.242(1)	374
		bcc	100	3.231(1)	391
		bcc	100	3.224(1)	404
		bcc	100	3.216(1)	450
		bcc	100	3.206(1)	25
$Al_{0.05}(TiVNb)_{0.85}Mo_{0.10}$	dihydride	*fcc*	96	4.398(1)	25
		bcc	4	3.330(1)	
	fcc + *bcc* mixture	*fcc*	95.5	4.401(1)	170
		bcc	4.5	3.336(1)	
		fcc	95	4.400(1)	184
		bcc	5	3.335(1)	
		fcc	88	4.396(1)	211
		bcc	12	3.320(1)	
		fcc	80	4.396(1)	220
		bcc	20	3.320(1)	
		fcc	65	4.395(1)	229
		bcc	35	3.320(1)	
		fcc	48	4.394(1)	238
		bcc	52	3.319(1)	
		fcc	25	4.391(1)	252
		bcc	75	3.317(1)	
		fcc	9	4.385(1)	265
		bcc	91	3.311(1)	
		fcc	3	4.382(1)	279
		bcc	97	3.303(1)	
	desorbed *bcc*	*bcc*	100	3.285(1)	297
		bcc	100	3.242(1)	328
		bcc	100	3.221(1)	351
		bcc	100	3.214(1)	364
		bcc	100	3.207(1)	400
		bcc	100	3.206(1)	450
		bcc	100	3.196(1)	25